



Contents lists available at ScienceDirect

Mechanical Systems and Signal Processing

journal homepage: www.elsevier.com/locate/ymssp

Review

Rolling element bearing diagnostics using the Case Western Reserve University data: A benchmark study

Wade A. Smith*, Robert B. Randall

School of Mechanical and Manufacturing Engineering, University of New South Wales, Sydney, NSW 2052, Australia

ARTICLE INFO

Article history:

Received 4 November 2014

Received in revised form

30 January 2015

Accepted 16 April 2015

Keywords:

Rolling element bearing

Bearing diagnostics

ABSTRACT

Vibration-based rolling element bearing diagnostics is a very well-developed field, yet researchers continue to develop new diagnostic algorithms quite frequently. Over the last decade, data from the Case Western Reserve University (CWRU) Bearing Data Center has become a standard reference used to test these algorithms, yet without any recognised benchmark it is difficult to properly assess the performance of any proposed diagnostic methods. There is, then, a clear need to examine the data thoroughly and to categorise it appropriately, and this paper intends to fulfil that objective. To do so, three established diagnostic techniques are applied to the entire CWRU data set, and the diagnostic outcomes are provided and discussed in detail. Recommendations are given as to how the data might best be used, and also on how any future benchmark data should be generated. Though intended primarily as a benchmark to aid in testing new diagnostic algorithms, it is also hoped that much of the discussion will have broader applicability to other bearing diagnostics cases.

© 2015 Elsevier Ltd. All rights reserved.

Contents

1. Introduction	3
2. Bearing diagnostics fundamentals	4
3. Experimental set-up	4
3.1. Test set-up	4
3.2. Description of data records	4
4. Use of the CWRU data in the literature	5
5. Diagnostic methods applied	5
5.1. Method 1: Envelope analysis of the raw signal	5
5.2. Method 2: Cepstrum prewhitening	5
5.3. Method 3: Benchmark method	6
6. Results and discussion	6
6.1. General observations of data sets	6
6.1.1. Discrete spectral components at high frequencies	7
6.1.2. Problems associated with data acquisition	9
6.2. Characterisation of all data sets	9

* Corresponding author. Tel.: +61 2 9385 4121; fax: +61 2 9663 1222.

E-mail address: wade.smith@unsw.edu.au (W.A. Smith).

6.3.	Drive end bearing faults, 12 kHz data (cf. Table B2)	10
6.3.1.	Inner race faults	10
6.3.2.	Ball faults	10
6.3.3.	Outer race faults, fault centred in load zone (6 o'clock)	14
6.3.4.	Outer race faults, fault orthogonal to load zone (3 o'clock)	16
6.3.5.	Outer race faults, fault opposite load zone (12 o'clock)	16
6.4.	Drive end bearing faults, 48 kHz data (cf. Table B3)	15
6.4.1.	Inner race faults	18
6.4.2.	Ball faults	18
6.4.3.	Outer race faults, fault centred in load zone (6 o'clock)	20
6.4.4.	Outer race faults, fault orthogonal to load zone (3 o'clock)	21
6.4.5.	Outer race faults, fault opposite load zone (12 o'clock)	22
6.5.	Fan end bearing faults, 12 kHz data (cf. Table B4)	23
6.5.1.	Inner race faults	23
6.5.2.	Ball faults	24
6.5.3.	Outer race faults, fault centred in load zone (6 o'clock)	25
6.5.4.	Outer race faults, fault orthogonal to load zone (3 o'clock)	25
6.5.5.	Outer race faults, fault opposite load zone (12 o'clock)	26
6.6.	Further discussion	27
6.7.	Summary of results	27
7.	Conclusions and recommendations	27
	Acknowledgements	31
	Appendix A Data set reference tables	31
	Appendix B Results tables	31

1. Introduction

Rolling element bearings (REBs) are one of the most prevalent components in rotating machines, and their failure is one of the most frequent reasons for machine breakdown. This has prompted a great deal of research on vibration-based diagnostics of REBs over the last few decades, and the area is now quite well understood, with a number of powerful diagnostic techniques available [1]. Yet researchers continually strive to develop improvements on the established diagnostic methods. Research of this nature benefits greatly from the availability in the public domain of reference data sets on which researchers can test their newly developed algorithms. The data set provided by the Case Western Reserve University (CWRU) Bearing Data Center [2] has become such a standard reference in the bearing diagnostics field, with the authors counting 41 papers using the CWRU data published in *Mechanical Systems and Signal Processing* between 2004 and early 2015.¹

Although this data is publicly available and widely used, there currently exists no benchmark against which the performance of new algorithms applied to the data can be assessed. Moreover, the CWRU data has its own unique characteristics: while some signals are dominated by classic bearing fault features, others are less clear or display other fault symptoms. For these reasons, there is a clear need for a benchmark study to provide a sound basis for properly assessing new diagnostic algorithms.

This paper provides such a benchmark by applying three established diagnostic techniques to the entire CWRU data set. The applied techniques range from very simple (envelope analysis of the raw vibration signal) to the so-called benchmark method, a variation on that described in ref. [1]. Every data record is studied and categorised, and many are discussed in detail. Much of this discussion will have broader applicability to other bearing diagnostics cases, and perhaps even to other areas of condition monitoring.

2. Bearing diagnostics fundamentals

Localised faults in rolling element bearings produce a series of broadband impulse responses in the acceleration signal as the bearing components repeatedly strike the fault. The precise location of the fault determines the nature of the impulse response series, and Fig. 1 shows the typical cases. A key point in bearing diagnostics is that the envelope signal, obtained via amplitude demodulation, typically contains clearer fault information than the raw signal, and so the corresponding envelope signals are also illustrated in the figure.

The primary tool for most bearing diagnostic techniques is the envelope spectrum, which reveals the repetition frequency of the impulse response series – one of the bearing ‘fault frequencies’ – as well as the nature of any modulation, which arises both from passage of the fault in and out of the load zone, and from the variation in transmission path from the fault to the (usually fixed) measurement point [3]. The three diagnostic techniques applied in this study are based on the

¹ Results cover from Volume 18 (3) (2004) up to and including Volumes 50–51 (January 2015).

Nomenclature		IR	inner race
		K	kurtosis
		M1–3	methods 1–3 (see Section 5)
		N	transform size (filter length)
		n	number of rolling elements
		N1, N2	unsuccessful diagnoses (see Table 4)
		OR	outer race
		P1, P2	partially successful diagnoses (see Table 4)
		Y1, Y2	successful diagnoses (see Table 4)
		Δ	delay used in discrete/random separation filter
		ϕ	angle of load from radial plane
BA	base plate acceleration		
BPFI	ball pass frequency, inner race		
BPFO	ball pass frequency, outer race		
BSF	ball (roller) spin frequency		
D	bearing pitch diameter		
d	rolling element diameter		
DE	drive end acceleration		
FE	fan end acceleration		
f_r	shaft speed		
FTF	fundamental train frequency (cage speed)		

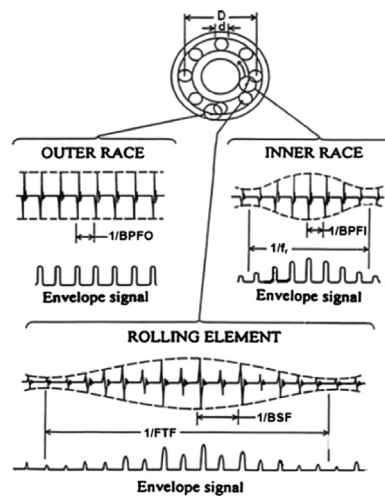


Fig. 1. Typical signals and envelope signals from local faults in rolling element bearings [1].

squared envelope spectrum (i.e., the spectrum of the squared envelope), the differences between them being the preprocessing steps applied, as outlined in Section 5. The bearing fault frequencies are as follows:

$$\begin{aligned}
 \text{Ball pass frequency, outer race:} & \quad BPFO = \frac{n f_r}{2} \left(1 - \frac{d}{D} \cos \phi\right) \\
 \text{Ball pass frequency, inner race:} & \quad BPFI = \frac{n f_r}{2} \left(1 + \frac{d}{D} \cos \phi\right) \\
 \text{Fundamental train frequency (cage speed):} & \quad FTF = \frac{f_r}{2} \left(1 - \frac{d}{D} \cos \phi\right) \\
 \text{Ball (roller) spin frequency:} & \quad BSF = \frac{D f_r}{2d} \left(1 - \left[\frac{d}{D} \cos \phi\right]^2\right)
 \end{aligned}$$

where f_r is the shaft speed, n is the number of rolling elements, and ϕ is the angle of the load from the radial plane. D , d , $BPFO$, $BPFI$, FTF and BSF are shown in Fig. 1. It is perhaps worth noting here that the f_r term is missing from the BSF equation in Ref. [1]. The fault frequencies above are based on kinematic relationships assuming no slip, but there is virtually always some slip, so a variation from the calculated frequency of up to 1–2% is common. Table 1 describes the expected envelope spectra based on the theory explained by McFadden and Smith [3] and outlined in Fig. 1.

3. Experimental set-up

3.1. Test set-up

The basic layout of the test rig is shown in Fig. 2. It consists of a 2 hp Reliance Electric motor driving a shaft on which a torque transducer and encoder are mounted. Torque is applied to the shaft via a dynamometer and electronic control system.

For the tests, faults ranging in diameter from 0.007 to 0.028 in. (0.18–0.71 mm) were seeded on the drive- and fan-end bearings (SKF deep-groove ball bearings: 6205-2RS JEM and 6203-2RS JEM, respectively) of the motor using electro-discharge machining (EDM). The faults were seeded on the rolling elements and on the inner and outer races, and each faulty bearing was reinstalled (separately) on the test rig, which was then run at constant speed for motor loads of 0–3

horsepower (approximate motor speeds of 1797–1720 rpm). Table 2 shows the relevant bearing details and fault frequencies. During each test, acceleration was measured in the vertical direction on the housing of the drive-end bearing (DE), and in some tests acceleration was also measured in the vertical direction on the fan-end bearing housing (FE) and on the motor supporting base plate (BA). The sample rates used were 12 kHz for some tests and 48 kHz for others, as explained further in Section 3.2. Further details regarding the test set-up can be found at the CWRU Bearing Data Center website [2].

3.2. Description of data records

Information for all 161 data sets is shown in the reference tables (Tables A1–A4) in Appendix A. It can be seen that the data sets are grouped into four categories – 48k baseline, 12k drive end fault, 48k drive end fault, and 12k fan end fault – according to the sample rate (12 or 48 kHz) and faulty bearing location. Within each group there are data sets for rolling element faults and inner and outer race faults, with the outer race faults themselves grouped into three categories according to the fault position relative to the load zone: ‘centred’ (fault in the 6.00 o’clock position), ‘orthogonal’ (3.00 o’clock) and ‘opposite’ (12.00 o’clock). It should be noted here that the only load borne by the bearings (in theory) is the static gravitational load from the weight of the shaft and any attached components, though as discussed in Section 6, there is evidence that there could be a dynamic load superimposed on this static load. The data sets are further categorised by fault size (0.007 to 0.028 in.) and motor load (0–3 hp).

Table 1

Expected pattern in envelope spectrum for various fault types.

Fault type	Expected components in envelope spectrum
Outer race	BPFO and harmonics, no sidebands
Inner race	BPFI and harmonics, sidebands spaced at f_r . Harmonics of f_r .
Rolling element (ball)	BSF and harmonics (even harmonics often dominant), sidebands spaced at FTF . Harmonics of FTF .

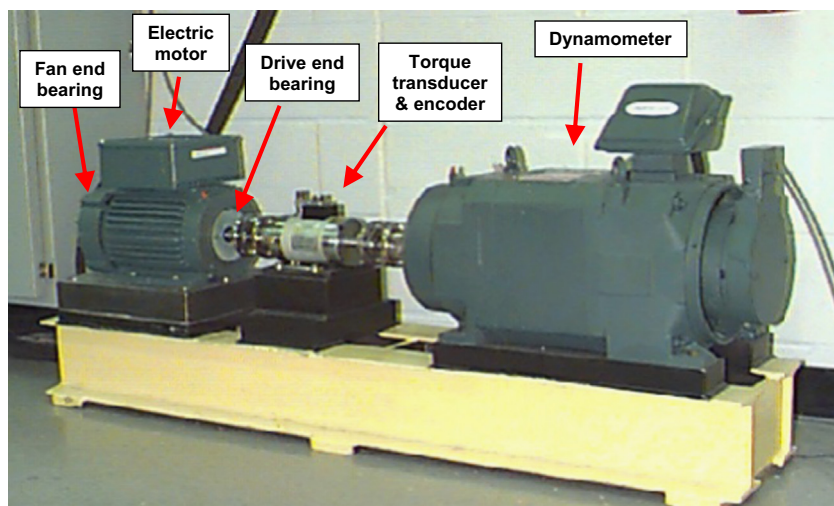


Fig. 2. CWRU bearing test rig [2].

Table 2

Bearing details and fault frequencies.

Position on rig	Model number	Fault frequencies (multiple of shaft speed)			
		BPFI	BPFO	FTF	BSF
Drive end	SKF 6205-2RS JEM ^a	5.415	3.585	0.3983	2.357
Fan end	SKF 6203-2RS JEM	4.947	3.053	0.3816	1.994

^a An equivalent NTN bearing was used for the 0.028 in. drive end faults.

4. Use of the CWRU data in the literature

As mentioned above, there are data sets for a number of different motor loads, i.e. torque loads applied by the dynamometer. Yet many papers overlook the point that ‘load’ here is virtually meaningless, since there is no mechanism (e.g., gears) to convert the torque to a radial load borne by the bearings. The primary effect of the motor load is on the shaft speed, which is reduced by almost 4% in the maximum load case, though this would have little effect on the diagnosability of the various data sets. Thus the only radial load on the bearings (in theory) is the static gravitational load acting through the 6.00 o'clock position (not the 3.00 o'clock position, as stated in one section of the CWRU website [2] and in a number of papers).

Most studies of the CWRU data seem to produce non-physical classifications from machine learning algorithms (e.g., [4,5]), yet as will be shown in Section 6, many of the data sets are dominated by non-classical features. Since these algorithms do not identify physical characteristics per se – rather variations from some baseline – there remains doubt over the broader applicability of some of the developed methods, especially in cases where data atypical of the bearing fault type has been used. Compounding this problem, many authors do not state the specific data sets and measurement points used in their analyses, making proper assessment of the merits of their methods near impossible.

5. Diagnostic methods applied

Three diagnostic methods were applied to the data sets in this study. All methods used the squared envelope spectrum (i.e., the spectrum of the squared envelope) as the final diagnostic tool, but different preprocessing steps were used before obtaining the envelope signal.

The methods, outlined below, are listed in order from the most simple to the most complex. For all data sets, Method 1 – envelope analysis of the raw signal – was first applied, and then only if Method 1 was found to be unsuccessful were Methods 2 and 3 applied. Since this study is intended primarily as a benchmark to aid in the testing of new diagnostic algorithms, there is little reason for applying complex methods to data that can be diagnosed from simple envelope analysis of the raw signal (Method 1).

5.1. Method 1: Envelope analysis of the raw signal

This method consisted simply of envelope analysis (squared envelope spectrum) of the full bandwidth raw signal. The justification for applying such a simple method is that there are no obvious masking sources in this case, and in fact many bearing faults were found to be easily diagnosable with this method. For such cases it means that the signals are not very demanding in terms of diagnostic power, and do not provide a good test for newly proposed algorithms (unless for specific purposes, such as the determination of fault size).

5.2. Method 2: Cepstrum prewhitening

This method consisted of the following steps:

1. Cepstrum prewhitening to set all frequency components to the same magnitude.
2. Envelope analysis (squared envelope spectrum) of the full bandwidth signal.

This method was first proposed in [6] and has been applied to variable speed applications in [7]. The basis of its functionality is that since all spectral bands have the same power spectral density, those with more impulsivity will tend to dominate the time records, and show impulsive responses that are typical of bearing faults. Resonances are also removed, but this can mean that resonances at frequencies that do not carry bearing fault information are less likely to mask those which do.

5.3. Method 3: Benchmark method

This method is a streamlined version of the benchmark method proposed in [1], which was based on the semi-automated bearing diagnostics procedure suggested in [8], and consisted of the following steps:

1. Discrete/random separation (DRS) to remove deterministic (discrete frequency) components.
2. Spectral kurtosis to determine the most impulsive band, followed by bandpass filtering.
3. Envelope analysis (squared envelope spectrum) of the bandpass filtered signal.

The separation of random and deterministic components was achieved using discrete/random separation (DRS) [9], which is based on the transfer function between the signal and a delayed version of itself. Ideally, such a function would be unity at the frequencies of discrete components, since they remain correlated regardless of time lag. Random components become less correlated with increasing delay, so, provided the delay time is well chosen, the transfer function would be close to zero for these frequencies. This transfer function, obtained directly in the frequency domain (using transform size

N), is then applied to the signal as a discrete/random separation filter. The DRS settings used in this paper – filter length N and delay Δ (in number of samples) – were established by trial and error on a small number of data sets, with $N=16384$ and $\Delta=500$ chosen for the 12k data and $N=8192$ and $\Delta=500$ used for the 48k data.

Spectral kurtosis was applied using Antoni's Fast Kurtogram [10].

6. Results and discussion

A discussion of the complete results set is given in Sections 6.2–6.5, with further discussion in Section 6.6, and a summary of results in Section 6.7. Before discussing the diagnosis outcomes for all the records, Section 6.1 below outlines a number of other characteristics observed in the data.

6.1. General observations of data sets

6.1.1. Discrete spectral components at high frequencies

On initial analysis of the records, discrete frequency components were observed over a wide frequency range in the spectra of many of the data sets. Fig. 3, from record 125DE (i.e., drive end), shows such an example. The raw time record on the left is quite unremarkable, with very stationary characteristics and a kurtosis of 3.04, but the PSD plot on the right shows discrete frequency components throughout much of the spectrum, especially in the 11–14 kHz band. After some investigation it was concluded that these components were attributable to two separate phenomena, one mechanical and one electro-magnetic.

The first effect, attributable to some mechanical phenomenon, was simply very high harmonics of shaft speed, which are often prominent in the 11–14 kHz region of the (48k data) spectra. It is not known whether these are true harmonics or rather sidebands spaced at shaft speed around some high-frequency carrier (at an integer multiple of shaft frequency). It seems most likely to be the former, and may be due to mechanical looseness, which can cause very sharp impacts represented in the spectrum by a large number of shaft harmonics.

The second effect was a series of high-frequency carrier-sideband families. Specifically, the carrier was found to be a series of harmonics of about 4.2 kHz, each with a number of sidebands spaced at, or slightly less than, shaft speed, or multiples thereof. These can be seen in Fig. 3(b), where the 4.2 and 8.4 kHz families are most pronounced.

The authors recently observed a similar phenomenon in data obtained from a test rig at the University of New South Wales (UNSW). In that case, the source of the discrete components was identified as being electro-magnetic interference (EMI) from a variable frequency drive (VFD) controlling an induction motor [11]. Such EMI is characterised by harmonics of a high frequency carrier (or 'switching frequency' in the pulse width modulated control signal, which is usually 2–15 kHz) surrounded by sidebands spaced at the control frequency (or 'pseudo-line frequency') sent to the motor [12]. In two-pole machines, the control frequency is equal to the synchronous speed, meaning that the sideband spacing in the EMI components is very close to shaft speed, with the latter being slightly less than the former due to slip. EMI from a variable frequency drive was at first suspected in the present case, yet this was not consistent with the later finding that the EMI sideband spacing was in fact *slightly less* than shaft speed.

After some consideration, it was concluded that the EMI source must have been the controller from the dynamometer, which is presumably an induction type generator. In such machines, torque is applied when the rotor (shaft) rotates *faster* than the synchronous speed (stator flux rotation), and the amount of torque is proportional to the slip between the two. Thus to achieve zero-load, the dynamometer would require no slip, and the flux frequency (control frequency for a two-pole machine) would be synchronous with the shaft speed. For non-zero load, some level of slip would be required, and the synchronous speed would be slightly less than shaft speed. This was observed to be the case here, where the dynamometer

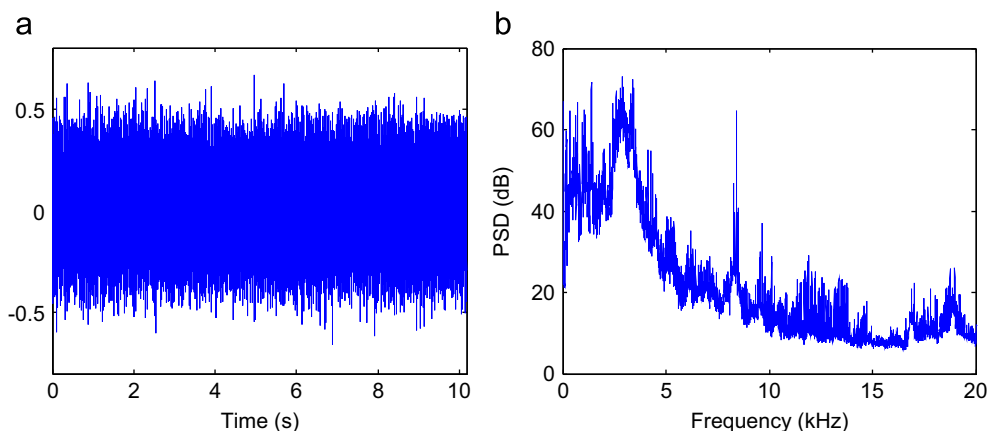


Fig. 3. Record 125DE (48k, 0.007 in. drive end ball fault, 1730 rpm). (a) Raw time signal. (b) Power spectral density.

appears to be a two-pole machine, such that the sideband spacing (control frequency) is at or slightly below shaft speed. The maximum slip level (at 3 hp) was found to be about 0.9%.

An interesting difference between motor- and generator-based EMI arises in the zero-load case. With an induction motor, even under a nominal zero load condition, there must exist some slip to overcome system losses, and so the EMI sideband spacing will never be equal to shaft speed (or an integer multiple thereof). Yet with a generator and controller, for a zero-load target, the control frequency would be exactly synchronous with shaft speed, such that the EMI sideband spacing would be at shaft speed (or integer multiples) and consequently may be difficult to differentiate from mechanical effects.

An example of the two effects – high shaft harmonics and EMI – is shown in Fig. 4, which is a zoomed version of the raw spectrum from record 125, the same data set as shown in Fig. 3. The figure shows a number of slightly smeared shaft harmonics, indicated by the red harmonic cursors spaced at $f_r = 28.68$ Hz. The EMI phenomenon is represented by very discrete components, indicated by the black cursors, where in this case the dominant spacing, at 113.65 Hz (4×28.41 Hz), is actually close to $4 \times f_r$ (although in other EMI component groups a spacing of $\sim f_r$ is present). Note that the EMI components here are not harmonics, but rather sidebands around a carrier frequency of about 12.54 kHz, believed to be the third harmonic of the switching frequency.

Even though it is generally desirable to analyse signals with a very wide frequency range for bearing diagnostics – to be sure of including those frequency ranges incorporating high frequency resonances excited by the bearing faults – due to these discrete components at high frequencies it seems that the lower frequency range data (with 12 kHz sampling frequency) might be easier to diagnose in this case. This is discussed further in subsequent sections.

6.1.2. Problems associated with data acquisition

A number of data sets show signs of problems associated with the data acquisition process itself, as outlined in Table 3. These records were treated in the same manner as all the others when carrying out the diagnostic analysis.

6.2. Characterisation of all data sets

The tables in Appendix B (Table B1–B4) give the diagnostic results from applying the methods outlined in Section 5. The diagnosis outcomes are categorised as shown in Table 4. Initially only Method 1 (raw signal) was applied to each data set, and then only if the diagnosis outcome was categorised as P1 or below were Methods 2 and 3 employed. Included in the tables is the kurtosis, K , of each raw data series (drive end measurement only), which in this case is defined as the normalised fourth order moment, rather than cumulant (i.e., $K=3$ for a Gaussian signal).

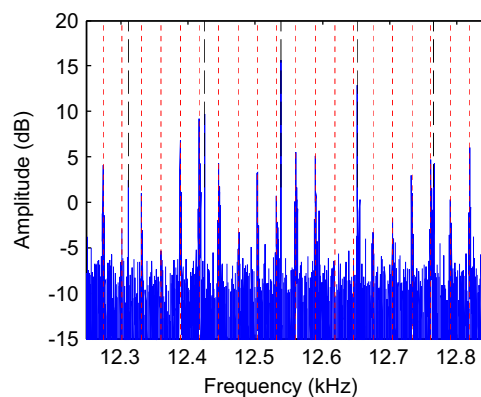


Fig. 4. Record 125DE (48k, 0.007 in. drive end ball fault, 1730 rpm), raw spectrum; finely tuned harmonic cursors at f_r (28.68 Hz) harmonics (red dot); finely tuned sideband cursors spaced at 113.65 Hz ($\sim 4 \times f_r$) around carrier at 12.54 kHz (black dash). (For interpretation of the references to colour in this figure legend, the reader is referred to the web version of this article.)

Table 3

Records affected by data acquisition problems.

Description of problem	Data sets affected
Records corrupted with patches of electrical noise	177 (DE and FE), 283 (DE, FE and BA)
Drive end and fan end measurements are identical except for a scaling factor of approximately 1.0154	189, 201, 213, 226, 238
Records appear to be clipped in sections	191DE, 214DE, 215DE, 228DE, 229DE, 236DE, 237DE

Table 4
Categorisation of diagnosis outcomes.

Diagnosis category	Diagnosis success	Explanation
Y1	Yes	Data clearly diagnosable and showing classic characteristics for the given bearing fault in both the time and frequency domains
Y2	Yes	Data clearly diagnosable but showing non-classic characteristics in either or both of the time and frequency domains
P1	Partial	Data probably diagnosable; e.g., envelope spectrum shows discrete components at the expected fault frequencies but they are not dominant in the spectrum
P2	Partial	Data potentially diagnosable; e.g., envelope spectrum shows smeared components that appear to coincide with the expected fault frequencies
N1	No	Data not diagnosable for the specified bearing fault, but with other identifiable problems (e.g., looseness)
N2	No	Data not diagnosable and virtually indistinguishable from noise, with the possible exception of shaft harmonics in the envelope spectrum

With respect to testing new bearing diagnostic algorithms, data sets in the Y categories would not provide a rigorous test since they are clearly diagnosable with well-established methods (unless there were some other benefits from using the proposed methods, e.g. computational efficiency). New algorithms might be tested by showing they can give a more comprehensive diagnosis of data sets in the P categories or by giving a successful diagnosis for data sets in the N categories.

One immediately apparent feature of the results shown in Appendix B is that the diagnosis outcomes seem to be less a function of the fault size or speed/load and more a function of the assembly, which was presumably the same for each fault size but then changed between fault sizes when a new bearing was installed. This is also reflected in the raw signal kurtosis values listed in the tables. As discussed throughout the following sections, it is suspected this phenomenon can be attributed to mechanical looseness, with a severity that changed with each bearing installation.

6.3. Drive end bearing faults, 12 kHz data (cf. Table B2)

6.3.1. Inner race faults

Many of the data sets in this category could be diagnosed by simple envelope analysis of the raw full bandwidth signal. Some, such as 209, show classic symptoms in both time and (envelope) spectral domains, as shown in Fig. 5.

Unless stated otherwise, the envelope spectra in this paper follow the convention established in Fig. 5(b), with a dotted-line data cursor at shaft speed, a dash-dot line at the first three harmonics of the expected fault frequency, and dotted lines illustrating the first order modulation sidebands (if any) around the first two harmonics of the fault frequency. Note that these are all at the calculated values based on the specified shaft speed (i.e., neglecting slip), and according to the sideband structures explained in Table 1.

The time signal in Fig. 5 shows a series of impulse responses at BPFI, amplitude modulated periodically at shaft speed, the rate at which the fault passes through the load zone. The envelope spectrum shows a series of harmonics of BPFI, with sidebands spaced at shaft speed around each harmonic, as well as a number of harmonics of the shaft speed.

Some others, such as 169, have a reasonably classical envelope spectrum (though with weak higher harmonics of BPFI), but an atypical time signal, as shown in Fig. 6.

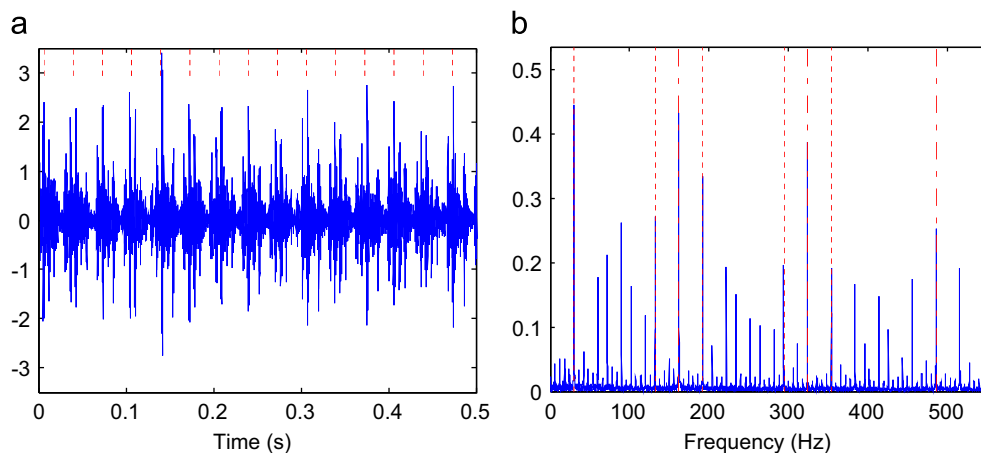


Fig. 5. Record 209DE (12k, 0.021 in. drive end inner race fault, 1797 rpm). (a) Raw time signal; cursors at $1/f_r$. (b) Envelope spectrum from Method 1 (raw signal); Y1 diagnosis.

The envelope spectrum in Fig. 6(b) still has harmonics of BPFI surrounded by sidebands spaced at shaft speed, though it will be seen that the spread of sidebands is greater than in Fig. 5(b), indicating a more impulsive modulation. However, the time signal in Fig. 6(a) no longer has obvious periodic modulation at shaft speed as in Fig. 5(a), but rather has a series of strong pulses spaced at approximately 1 revolution. On closer inspection, the pulses are found to be spaced at multiples of $1/\text{BPFI}$, but with a very impulsive modulation at shaft speed. As will be discussed later in connection with outer race faults, it is suspected that this could be a result of mechanical looseness, causing impulsive modulation of random amplitude at intervals of one revolution, but not necessarily phase-locked to the rotation.

There are other similar cases where the second harmonic of shaft speed (and corresponding sidebands) dominate over the first order in the envelope spectra, but the diagnosis of an inner race fault is still clear.

Records 3001 – 3004 (0.028 in.), using NTN rather than SKF bearings, could not be diagnosed correctly, but consistently gave strong discrete components in the envelope spectrum at $3.68 \times$ and $4.29 \times$, which do not match any of the fault frequencies of either the drive end or fan end bearings.

6.3.2. Ball faults

The ball fault cases are certainly the most difficult to diagnose, with only few giving the classic envelope spectrum symptoms of harmonics of BSF (possibly with dominant even harmonics) surrounded by modulation sidebands at cage speed (FTF), and with corresponding low harmonics of FTF. The only data sets diagnosable from direct envelope analysis of the raw signal (Method 1) are from the 0.021 in. and 0.028 in. fault cases.

One of the clearest is data set 3007DE, which, though diagnosable with Method 1, gave quite classic characteristics when processed using Method 3 (benchmark), as shown in Fig. 7. The strongest ball-fault harmonics are at 2 and 4 times BSF, with sidebands spaced at FTF (second order sidebands strongest). There are also at least three harmonics of FTF.

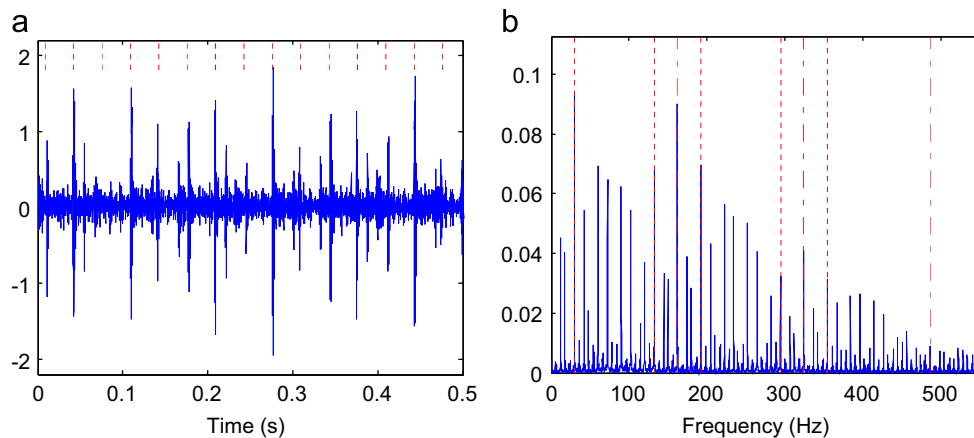


Fig. 6. Record 169DE (12k, 0.014 in. drive end inner race fault, 1797 rpm). (a) Raw time signal; cursors at $1/f_r$. (b) Envelope spectrum from Method 1 (raw signal); Y2 diagnosis.

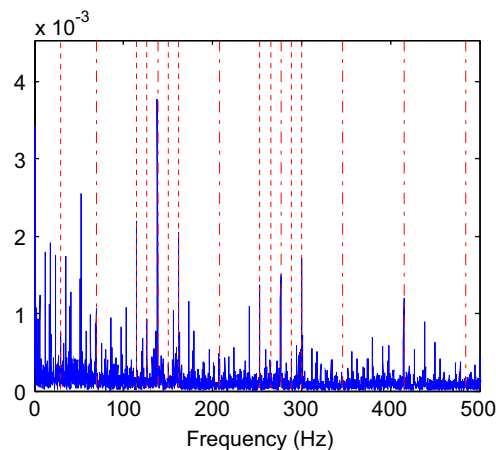


Fig. 7. Record 3007DE (12k, 0.028 in. drive end ball fault, 1750 rpm). Envelope spectrum from Method 3 (benchmark); cursors at: f_r (red dot), BSF harmonics (red dash-dot), sidebands spaced at FTF around $2 \times \text{BSF}$ and $4 \times \text{BSF}$ (red dot); Y1 diagnosis. (For interpretation of the references to colour in this figure legend, the reader is referred to the web version of this article.)

A number of other cases seem to exhibit special ratios of the fundamental bearing frequencies and are consequently difficult to diagnose. For example, Fig. 8 shows the envelope spectrum for data set 118DE, where all significant components seem to be harmonics of $0.2 \times f_r$. It is quite likely in this case that the amount of mean slip in the bearing has adjusted itself to lock onto an exact subharmonic of a dominant frequency such as shaft speed, with FTF here seeming to lock onto $0.4 \times$ (theoretical value $0.3983 \times$) and the resulting sum and difference frequencies all falling on $0.2 \times$ harmonics. A further possibility is that the local slip affecting BSF, with a theoretical value of $2.357 \times f_r$, has adjusted to lock onto one of these $0.2 \times$ harmonics ($2.2 \times$ or $2.4 \times$). With a strong component at $2.4 \times$ in Fig. 8, a tentative diagnosis could be made on that basis. It is difficult to explain, however, why the odd BSF components in the envelope spectrum are much stronger than the even ones, so the case has been listed as an N1 diagnosis.

Another interesting feature of many of the ball fault data sets is that there is often evidence of outer and inner race faults. Fig. 8 for example shows strong components at $3.6 \times$ and especially $7.2 \times f_r$, which corresponds exactly to the first and second harmonics of BPFO if FTF is indeed $0.4 \times f_r$. But there is also a strong component at $5.4 \times f_r$, which is very close to BPFI (theoretical value $5.415 \times$). This raises an interesting point about bearing fault frequencies in the presence of slip. The fundamental definition of BPFO (assuming a fixed outer race) is simply the cage speed multiplied by the number of rolling elements, i.e. $BPFO = n \times FTF$, while BPFI is defined by the relative speed between the cage and the inner race, or $BPFI = n \times (f_r - FTF)$. This means the sum of BPFO and BPFI must always be $n \times f_r$, regardless of the level of slip.

In the present case, with nine rolling elements, it means that if BPFO has increased to $3.6 \times f_r$ through slip, then BPFI must decrease to $5.4 \times f_r$, and the cage speed must be $0.4 \times f_r$, which corresponds well to Fig. 8 (the possibility of local slip means that BSF could in theory take on any value). The same effect could also be caused by a change in load angle: with $\phi \approx 10^\circ$, the kinematic fault frequencies for the drive end bearing listed in Table 2 become $5.4 \times$, $3.6 \times$, $0.4 \times$ and $2.36 \times$ (BPFI, BPFO, FTF and BSF). The first explanation, with the slip adjusting to lock onto a dominant frequency, seems the more likely of the two,

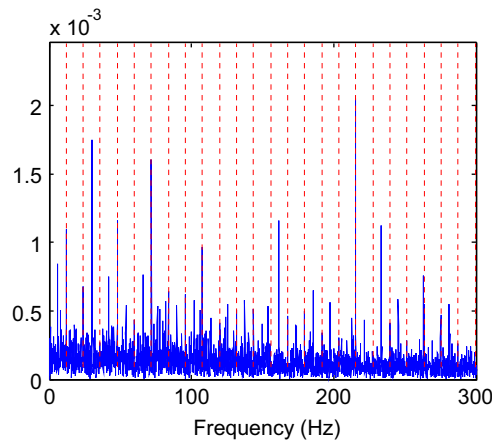


Fig. 8. Record 118DE (12k, 0.007 in. drive end ball fault, 1797 rpm). Envelope spectrum from Method 1 (raw signal); finely tuned cursors at FTF (shown to be $0.4 \times f_r$); N1 diagnosis.

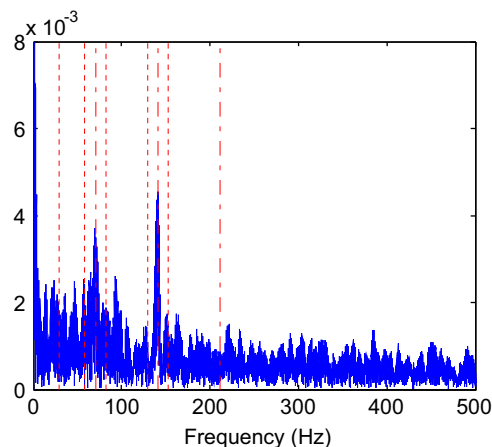


Fig. 9. Record 222DE (12k, 0.021 in. drive end ball fault, 1797 rpm). Envelope spectrum from Method 3 (benchmark); Y2 diagnosis.

however, as there is no reason for a thrust force in this case.

Many of the remaining 0.007 in. fault cases exhibit similar characteristics, most notably in the drive end measurements.

Yet another interesting feature in the ball fault cases – observed to varying extents with the 0.014 in. and 0.021 in. faults – is that of smeared components in the envelope spectrum corresponding most notably to $2 \times \text{BSF}$, but also to other BSF harmonics. An example of this is shown in the envelope spectrum in Fig. 9, from 222DE processed with Method 3 (benchmark). The smearing was first thought to have been caused by random slip of the balls, especially in connection with the discussion above regarding the slip adjusting so as to lock onto a dominant frequency. But in fact, on inspection of the raw time signal – shown alongside the corresponding envelope spectrum in Fig. 10 – the cause of the smeared BSF components can clearly be attributed to random, impulsive amplitude modulation rather than ball slip (phase modulation). Each large pulse in the figure consists of impulse responses corresponding to BSF ($2 \times$ in particular). This may be due to the fault only contacting the races at those times, possible with ball (and not roller) bearings since the ball is free to rotate about any axis.

A final observation from Fig. 10 is in relation to the discrete components in the envelope spectrum, which actually correspond to BPFO and BPFI, the latter even with clear sidebands spaced at shaft speed. That these components are discrete means the corresponding content in the time signal is not subject to the same random and impulsive amplitude modulation as the BSF-related pulses; they are rather part of the stationary portion of the signal. This also explains why the discrete components were not found in the envelope spectrum from Method 3 (benchmark) in Fig. 9 – spectral kurtosis would tend to enhance only the large BSF-related pulses, which stand out from the remainder of the signal and thus have very high kurtosis. Nor was Method 2 (cepstrum prewhitening) able to diagnose the (unintended) inner and outer race faults in this case.

Unintended faults in both races perhaps suggests brinelling, which can be caused by excessive load when stationary (true brinelling), but also by vibration (false brinelling) during either transportation or on standby [13]. One possibility is that the races were unintentionally damaged by brinelling when dismantling or reassembling the bearings for seeding the faults.

6.3.3. Outer race faults, fault centred in load zone (6 o'clock)

Only a relatively small number of cases exhibit normal characteristic symptoms of a simple outer race fault, with harmonics of BPFO in the envelope spectra, and little in the way of modulation sidebands (or other harmonics) since the fault is in the load zone and thus the conditions are in principle the same for the passage of all rolling elements. The time signal should exhibit a series of reasonably uniform impulse responses from the passage of each ball over the fault. The cases marked Y1 do have these characteristics, with only small modulation sidebands or other harmonics. They are for all cases with the smallest fault (0.007 in.), at all measurement positions, and at all speeds. This again suggests that assembly is more of a factor than fault size or speed/load in determining the nature of the diagnosis.

Fig. 11 is a typical example showing the raw time signal and corresponding envelope signal for data set 133DE. The series of impulse responses corresponds to BPFO, and even though there is a small amount of modulation at shaft speed and cage speed, it does not distort the diagnosis.

Most of the next four series of data, for fault size 0.014 in., could not be diagnosed by any of the techniques applied. Some records contain seemingly random pulses, again perhaps attributable to mechanical looseness. Fig. 12 shows an example of this from data set 200, with the same speed/load as data set 133 (Fig. 11).

The only case for 0.014 in. fault size with a partial diagnosis is data set 197, using the benchmark method, for which the processed time signal and corresponding envelope spectrum are shown in Fig. 13. Harmonics of BPFO can be seen, surrounded by sidebands at cage speed. There are strong harmonics at cage speed, and modulation at this frequency is the only characteristic that can be seen in the time signal.

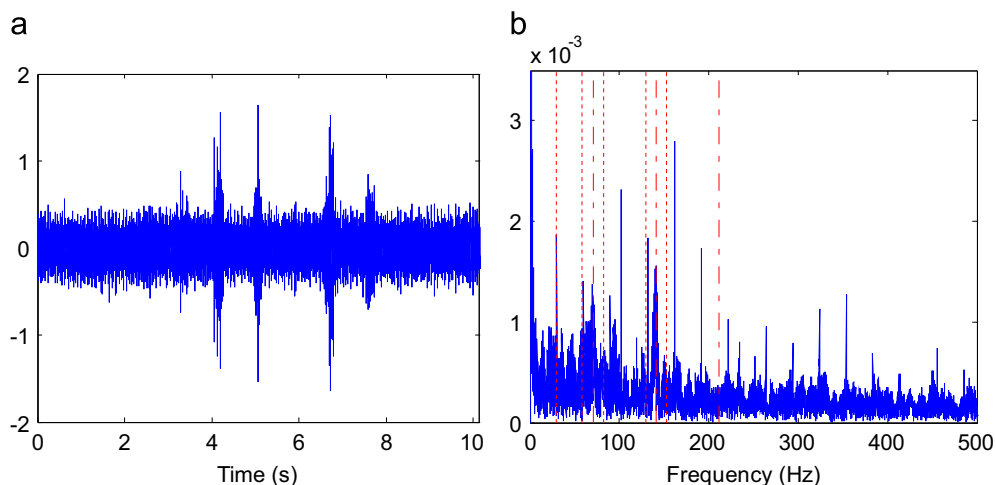


Fig. 10. Record 222DE (12k, 0.021 in. drive end ball fault, 1797 rpm). (a) Raw time signal. (b) Envelope spectrum from Method 1 (raw signal); P1 diagnosis.

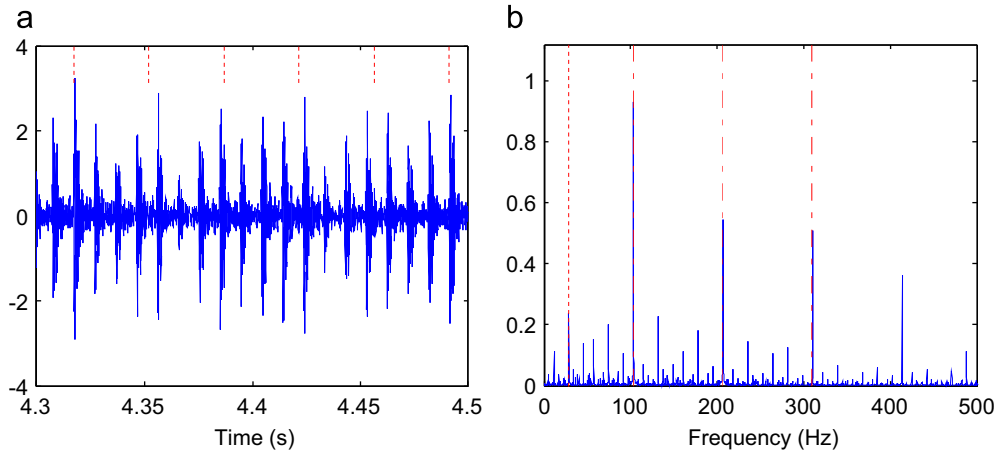


Fig. 11. Record 133DE (12k, 0.007 in. drive end outer race fault centred, 1730 rpm). (a) Raw time signal; cursors at $1/f_r$. (b) Envelope spectrum from Method 1 (raw signal); Y1 diagnosis.

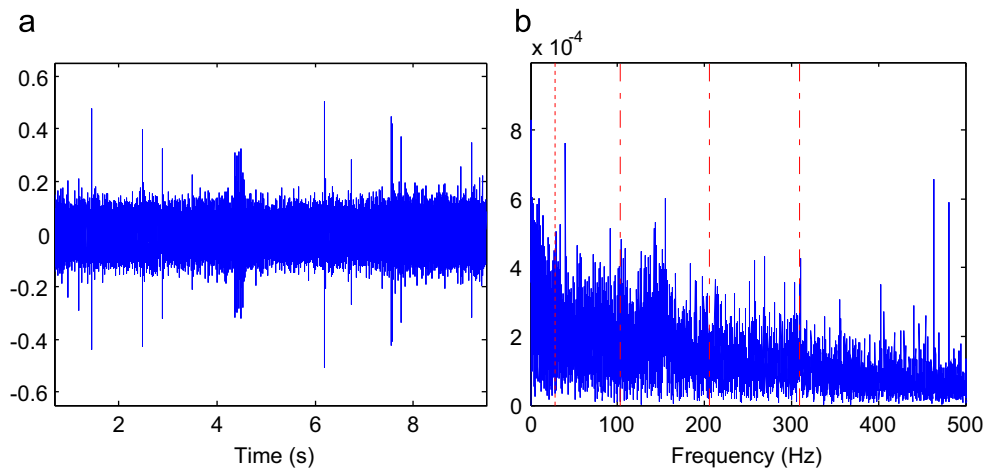


Fig. 12. Record 200DE (12k, 0.014 in. drive end outer race fault centred, 1730 rpm). (a) Time signal from Method 3 (benchmark). (b) Corresponding envelope spectrum; N1 diagnosis.

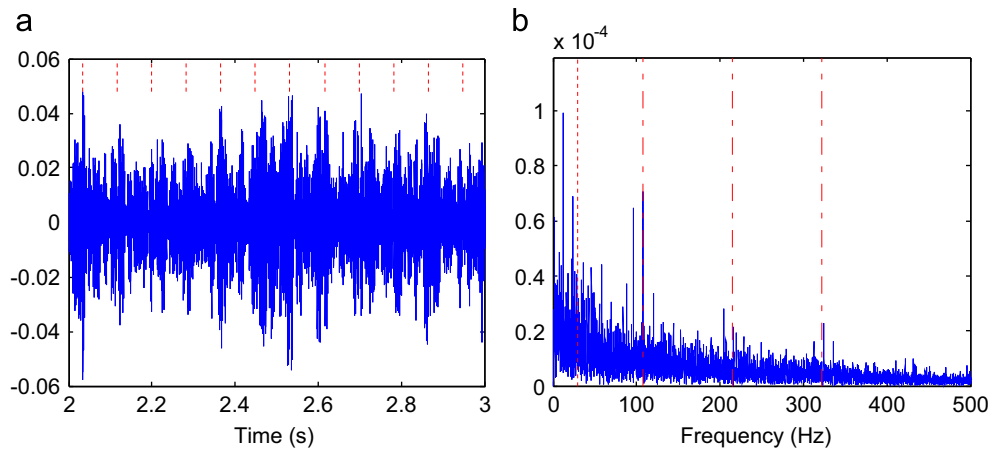


Fig. 13. Record 197DE (12k, 0.014 in. drive end outer race fault centred, 1797 rpm). (a) Time signal from Method 3 (benchmark); cursors at $1/FTF$. (b) Corresponding envelope spectrum; Y2 diagnosis.

All the remaining data sets (0.021 in. fault size) have been marked as Y2 diagnoses, because even though they have clear harmonics of BPFO in the envelope spectrum, the latter are surrounded by strong sidebands at shaft speed, and there are also corresponding low harmonics at shaft speed.

A typical case is represented by data set 235, for which a typical time record and envelope spectrum are given in Fig. 14. As with record 169, discussed in Section 6.3.1 and shown in Fig. 6, the time signal in Fig. 14(a) actually does contain pulses corresponding to the fault frequency (1/BPFO in this case), but they are subject to a very impulsive modulation at shaft

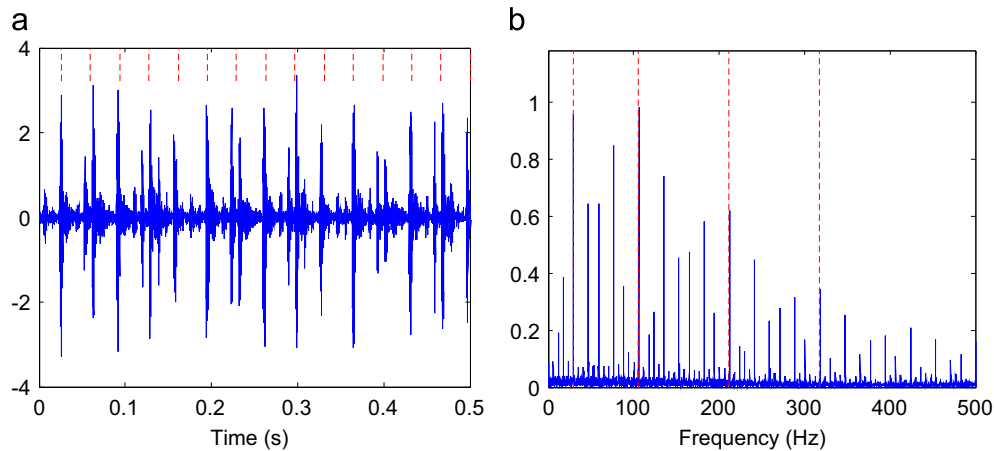


Fig. 14. Record 235DE (12k, 0.021 in. drive end outer race fault centred, 1772 rpm). (a) Raw time signal; cursors at $1/f_r$. (b) Envelope spectrum from Method 1 (raw signal); Y2 diagnosis

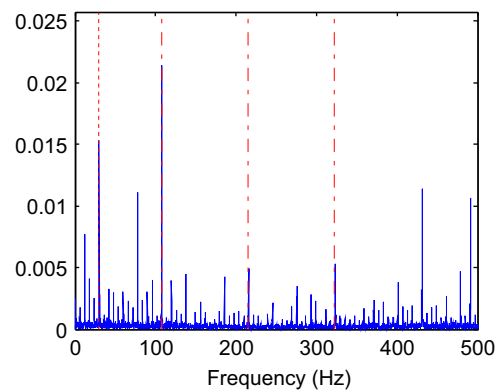


Fig. 15. Record 144FE (12k, 0.007 in. drive end outer race fault orthogonal, 1797 rpm). Envelope spectrum from Method 1 (raw signal); Y2 diagnosis.

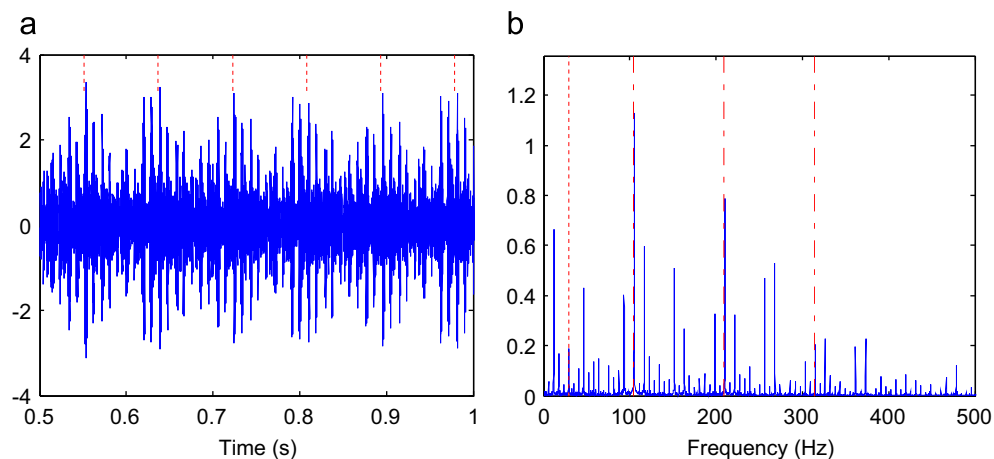


Fig. 16. Record 146DE (12k, 0.007 in. drive end outer race fault orthogonal, 1750 rpm). (a) Raw time signal; cursors at $1/FTF$ (b) Envelope spectrum from Method 1 (raw signal); Y2 diagnosis.

speed. Strong modulation of outer race fault signals suggests a rotating load, for which the most likely explanation appears to be mechanical looseness, which is known to give impulsive shocks with spectra containing multiple harmonics of shaft speed. It is not a smooth modulation such as might be given by a strong unbalance rotating with the shaft.

It can be seen in Fig. 14 that there are also sidebands spaced at FTF and shaft speed minus FTF.

6.3.4. Outer race faults, fault orthogonal to load zone (3 o'clock)

All cases for the 0.007 in. fault were diagnosable with Method 1 (raw signal), but although they all show strong harmonics of BPFO, they are all modulated to some extent by shaft speed, FTF or both, giving a mix of Y1 and Y2 diagnoses depending on the degree of modulation. Fig. 15 is for data set 144FE and has perhaps the most modulation at shaft speed, whereas Fig. 16 is for data set 146DE, where the modulation is dominated by cage speed (FTF). Fig. 16(a) shows the time record, where the modulation at cage speed is very clear, even in the raw signal, while Fig. 16(b) shows the envelope spectrum with harmonics of BPFO surrounded by sidebands at FTF.

The only other data sets are for 0.021 in. fault size (records 246–249), for which the diagnosis results are a mix of the Y2 and P1 categories, since in all cases there are strong harmonics of shaft speed, and sidebands spaced at shaft speed around the harmonics of BPFO. Many of the envelope spectra also contain harmonics of $0.2 \times f_r$, as discussed in Section 6.3.2 in relation to ball faults. In some cases these $0.2 \times$ components are so strong that they interfere with the diagnosis. Fig. 17, from record 246BA, shows such a case, which has been marked as a P1 diagnosis due to the weakness of the BPFO component relative to other $0.2 \times$ harmonics. Again, the nature of the modulation in Fig. 17(a) is consistent with mechanical looseness.

6.3.5. Outer race faults, fault opposite load zone (12 o'clock)

In theory, it should not be possible to get any response to a fault located outside the load zone, because there will be no contact between the rolling elements and the fault, but in the data analysed here there is obviously some response at the

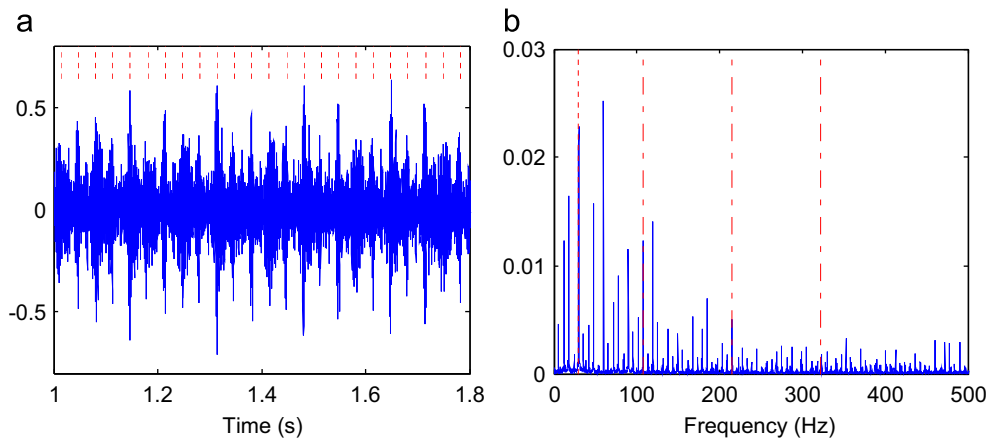


Fig. 17. Record 246BA (12k, 0.021 in. drive end outer race fault orthogonal, 1797 rpm). (a) Raw time signal; cursors at $1/f_r$. (b) Envelope spectrum from Method 1 (raw signal); P1 diagnosis.

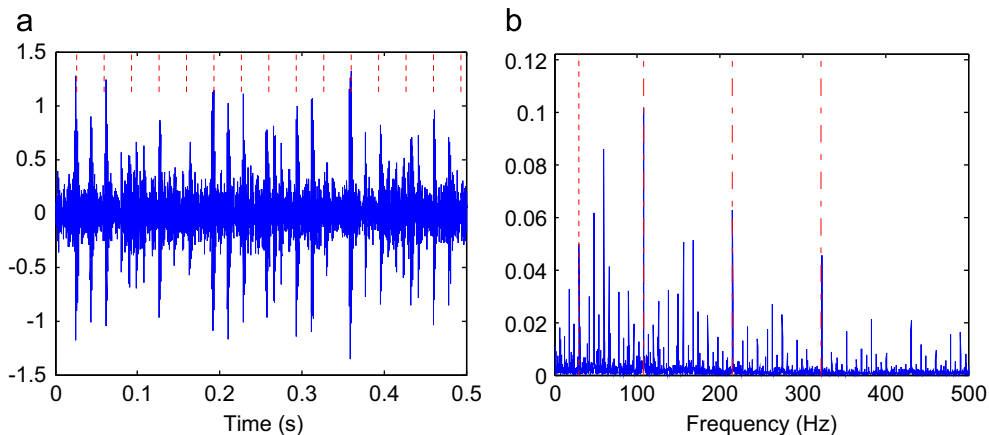


Fig. 18. Record 156DE (12k, 0.007 in. drive end outer race fault opposite, 1797 rpm). (a) Raw time signal; cursors at $1/f_r$. (b) Envelope spectrum from Method 1 (raw signal); Y2 diagnosis.

bearing fault frequency in many cases.

Only two fault sizes are tested, 0.007 in. and 0.021 in., and most give Y2 or P1 diagnoses for all speeds and measurement points. Even though harmonics of BPFO are found in all these cases, there are also harmonics of shaft speed, and sidebands spaced at shaft speed. In the case of data set 156DE, the second harmonic of shaft speed is stronger than the first, as are the corresponding sidebands, as shown in Fig. 18(b). In the corresponding time record in Fig. 18(a), there are seen to be sections of signal with pulses spaced corresponding to twice shaft speed, though not continuously. There are separate patches of signal with pulses spaced at BPFO. Since the fault can only produce a response when loaded, this means that the load zone is not fixed at the bottom of the bearing (6 o'clock) but varying as the shaft moves around, most likely because of mechanical looseness. Some sidebands spaced at FTF and shaft speed minus FTF are also visible in Fig. 18(b), and corresponding low frequency modulations are also seen in the time record.

Somewhat remarkably, a few data sets were found to give classic symptoms of BPFO when analysed by Method 2, based on cepstral prewhitening. It appears that this removes some of the other effects giving modulations at other frequencies. Fig. 19 gives an example from data set 156 (same record as Fig. 18), where now the time record is dominated by weak occasional pulses spaced at BPFO, and the envelope spectrum is dominated by the harmonics of BPFO. However, it is obvious that the situation is far from that of a typical outer race fault as depicted in Fig. 11 in Section 6.3.3.

The kurtosis figures for the 0.021 in. fault sizes given in Table B2 – values in the range 33–35, much larger than the other outer race fault cases – again highlight that assembly is the dominant factor in determining the nature of the measured signals. As with some earlier cases discussed above, impulsive modulation (at shaft speed) of the fault frequency was again apparent in these cases (data sets 258–261).

6.4. Drive end bearing faults, 48 kHz data (cf. Table B3)

6.4.1. Inner race faults

The smallest and largest faults (0.007 in. and 0.021 in.) in this category were all diagnosable using Method 1 (raw signal). Some of these have been categorised as Y1 diagnoses, but most have been listed as Y2 due primarily to two non-classical symptoms in the envelope spectrum: strong $2 \times f_r$ harmonics and sidebands around BPFI, and strong FTF harmonics and sidebands around BPFI. An example of the former is shown in Fig. 20, which is from data set 109.

Diagnosis was found to be most difficult with the data sets from the 0.014 in. fault (sets 174–177), which were found – as with the corresponding 12k cases – to exhibit impulsive shaft speed modulation of the bearing fault frequency (BPFI). It was previously argued that this is likely due to mechanical looseness, and further evidence of an assembly problem is borne out in the (near) consecutiveness of the record numbers: the 12k data sets 169 to 172 – presumably recorded with the same assembly but a different sample rate – were also very impulsive.

An example of this is shown in Fig. 21, from record 176, which has similarities with 12k set 169 (Fig. 6). The strongest components in the envelope spectrum are $2 \times f_r$ and the $3 \times f_r$ sideband on the left side of BPFI. The pulses in the time domain are spaced at multiples of $1/\text{BPFI}$, with very clear impulsive modulation at shaft speed.

On the other hand, Fig. 22 shows the results from data set 174, which is also very impulsive but was not diagnosable with any of the techniques applied. The spacing of the pulses and their modulation in this case seem quite random and are certainly not related to shaft speed or BPFI.

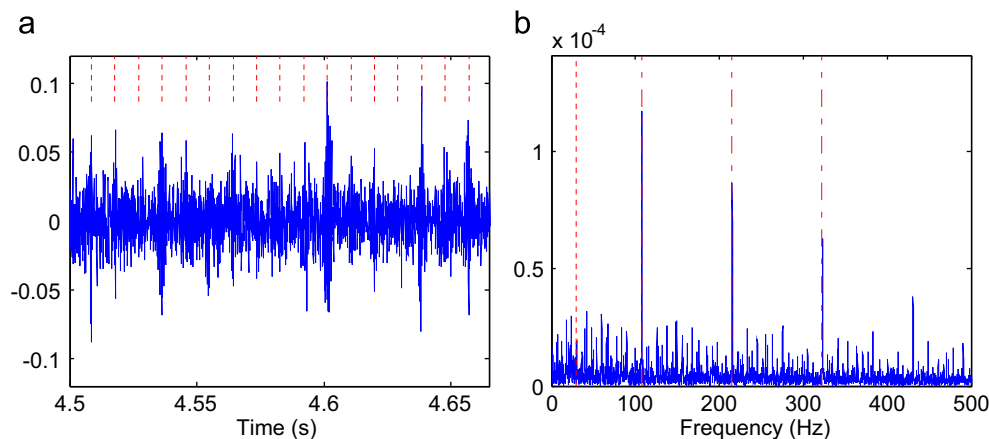


Fig. 19. Record 156DE (12k, 0.007 in. drive end outer race fault opposite, 1797 rpm). (a) Time signal from Method 2 (prewhitening); cursors at $1/\text{BPFO}$. (b) Corresponding envelope spectrum; Y1 diagnosis.

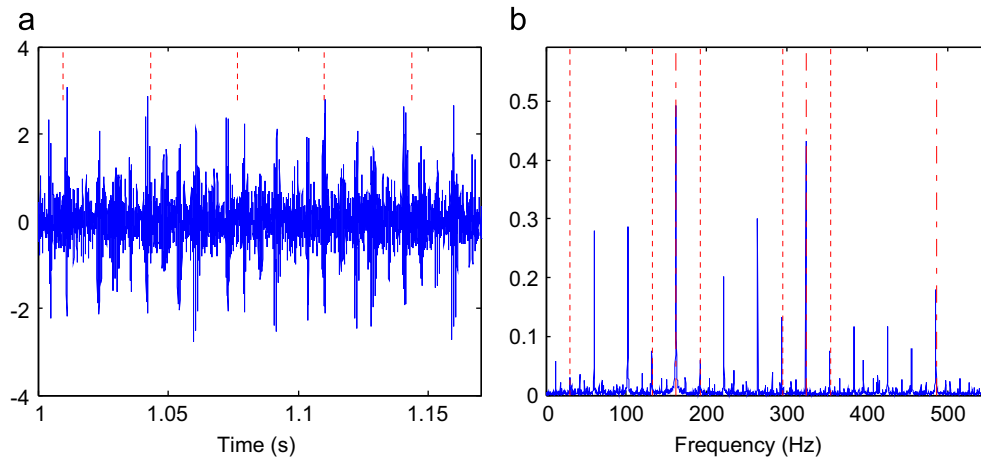


Fig. 20. Record 109DE (48k, 0.007 in. drive end inner race fault, 1797 rpm). (a) Raw time signal; cursors at $1/f_r$. (b) Envelope spectrum from Method 1 (raw signal); Y2 diagnosis.

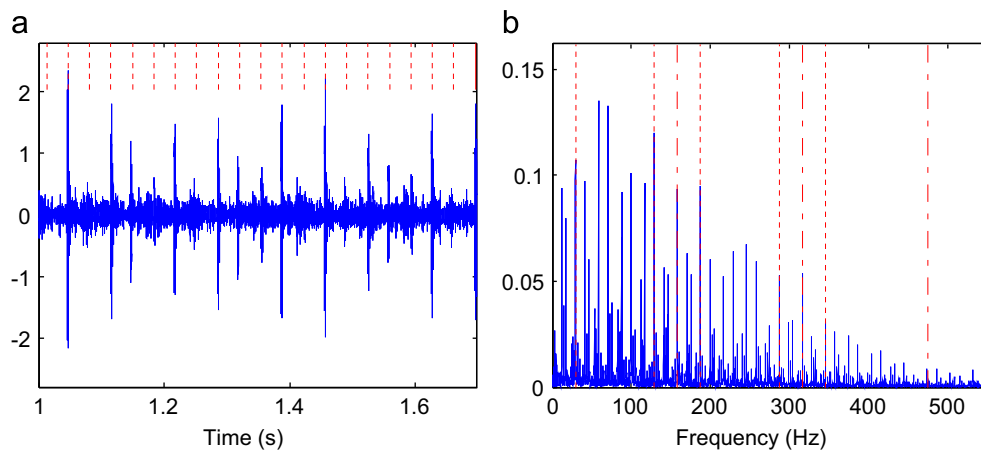


Fig. 21. Record 176DE (48k, 0.014 in. drive end inner race fault, 1750 rpm). (a) Raw time signal; cursors at $1/f_r$. (b) Envelope spectrum from Method 1 (raw signal); P1 diagnosis.

6.4.2. Ball faults

As with the 12k data, the ball faults were found to be by far the most difficult to diagnose correctly. Many of the data sets have impulsive content that is unrelated to the specified bearing fault. An example is shown in Fig. 23, from record 191, which did not give a successful diagnosis. It can be seen here that the signal is very non-stationary, and on closer inspection pulses with spacing corresponding to $2 \times \text{BSF}$ can be seen in the time signal around the 2 s mark, but this information is masked in the envelope spectrum by other effects, again probably arising from mechanical looseness. It may of course be the case here that the ball fault is only engaging with the races in that part of the signal. However, closer inspection of other impulsive parts of the signal – around the 0.4 s mark, for example – reveals a dominant spacing corresponding to BPFO (~ 104 Hz), and this is what dominates the envelope spectrum. As discussed in Section 6.3.2, the apparent smearing of these components in the envelope spectrum is due not to phase modulation (slip), but rather to amplitude modulation of the impulse responses by a seemingly random phenomenon. Another explanation for occasional pulses with spacings alternating between different bearing fault periods is that some loose foreign material is present in the bearing, which becomes lodged on one component, then dislodges before resettling on another, and so on.

Fig. 24 shows record 227, which gives a partial diagnosis. Similar to data set 222, discussed in Section 6.3.2, the envelope spectrum shows smeared components that correspond to BSF and in particular $2 \times \text{BSF}$. The time plot again reveals amplitude modulation of impulse responses by a phenomenon that is itself very impulsive and seemingly random. The individual impulse response spacing within the larger pulses corresponds to $2 \times \text{BSF}$. As with record 222 in Fig. 10, there is also a discrete component at BPFI in the envelope spectrum, suggesting an inner race fault whose resulting impulse responses are not subject to the same random modulation effect.

These smeared BSF characteristics were observed in the envelope spectra from all processing methods with data set 227, but a variation on this was observed with data set 226, as shown in Fig. 25. The envelope spectrum from Method 1 (raw

signal) is dominated by discrete components, but not at BSF or its harmonics (N1 diagnosis). Yet the envelope spectrum from Method 2 (cepstrum prewhitening) reveals smeared components as found with record 227, this time most notably at $2 \times \text{BSF}$, but also at $4 \times \text{BSF}$ and $8 \times \text{BSF}$ (P1 diagnosis). The envelope spectrum from Method 1 also shows discrete components at both BPFO and BPFI, and a discrete component at BPFI can also be seen in the envelope spectrum from

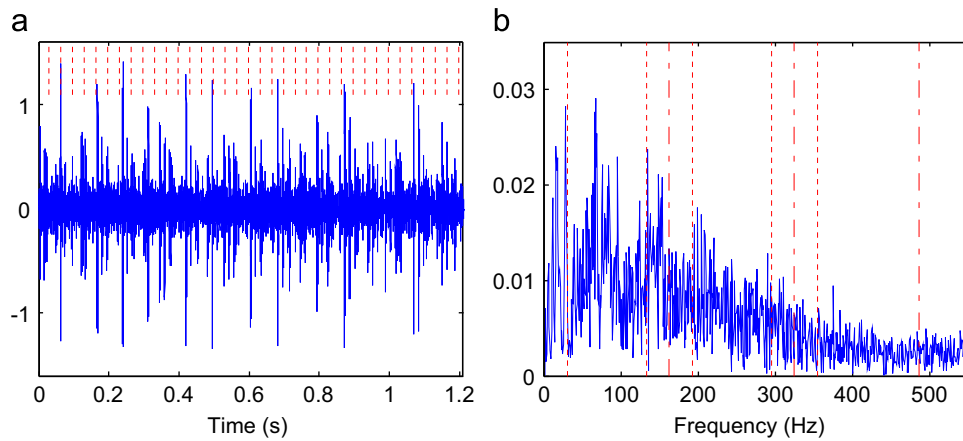


Fig. 22. Record 174DE (48k, 0.014 in. drive end inner race fault, 1797 rpm). (a) Raw time signal; cursors at $1/f_r$. (b) Envelope spectrum from Method 1 (raw signal); N1 diagnosis.

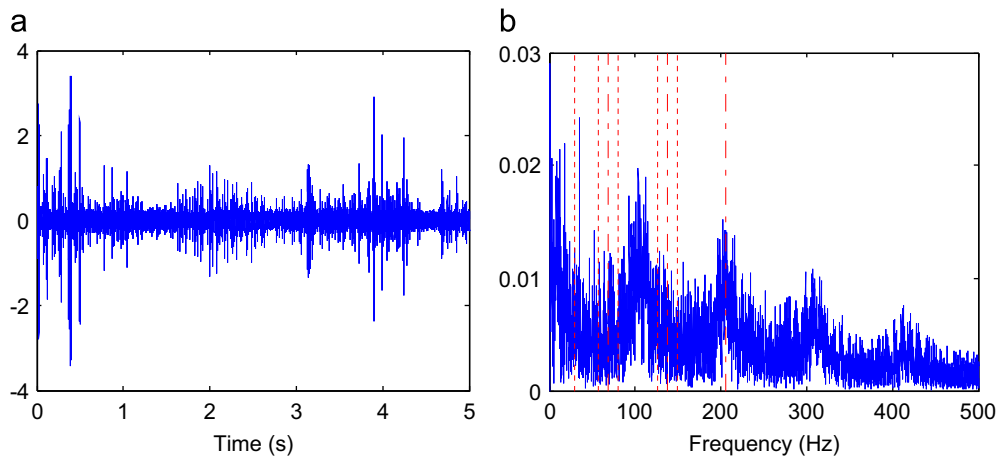


Fig. 23. Record 191DE (48k, 0.014 in. drive end ball fault, 1750 rpm). (a) Raw time signal. (b) Envelope spectrum from Method 1 (raw signal); N1 diagnosis.

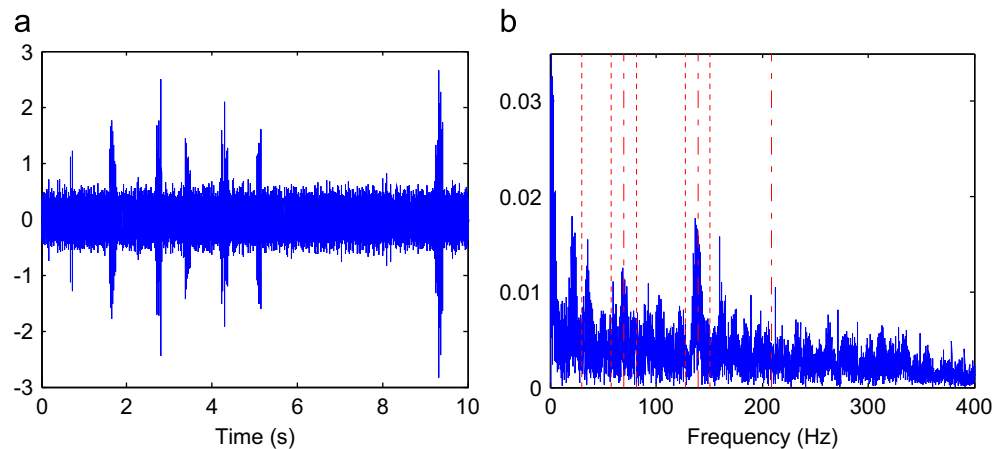


Fig. 24. Record 227DE (48k, 0.021 in. drive end ball fault, 1772 rpm). (a) Raw time signal. (b) Envelope spectrum from Method 1 (raw signal); P1 diagnosis.

Method 2. This supports the findings in Section 6.3.2 that (unintended) outer and inner race faults are present in the drive end bearing, perhaps caused by brinelling.

It therefore seems clear that, as with the 12k data, successful diagnosis of these ball faults is hampered firstly by a random, impulsive modulating effect, and secondly by the presence of faults on both races. The former effect results in smearing in the envelope spectrum corresponding to the modulated pulses, yet not all impulse response groups are subject to this modulation in every record, as shown in Fig. 25 (record 226DE), which shows spectral components that are discrete at BPFI and BPFO but smeared at $2 \times \text{BSF}$.

6.4.3. Outer race faults, fault centred in load zone (6 o'clock)

Data sets 135–138 show quite classic characteristics and give the clearest diagnoses of this group, which is counter-intuitive given that they represent the smallest fault (0.007 in.). This – combined with the same finding from the 12k data and the point made in Section 6.4.1 regarding the consecutiveness of the record numbers – again suggests that assembly is more of an issue than the fault itself.

The 0.014 in. faults (records 201–204) give mixed results, with diagnoses ranging from the N2 to Y2 categories. Again, most of the records show impulse responses subject to impulsive amplitude modulation, an example of which is given in Fig. 26, from record 203. As noted in the previous section, amplitude modulation of this nature gives rise to smearing effects in the envelope spectrum, which can be clearly seen in the figure.

The 0.021 in. faults (records 238–241) give very similar results to the corresponding records from the 12k data, with the envelope spectra giving clear BPFO components with strong sidebands spaced at shaft speed. There are also sidebands spaced at FTF around both shaft and BPFO harmonics. Fig. 27 shows the results from data set 239, which matches the corresponding 12k record, 235, very closely (see Fig. 14).

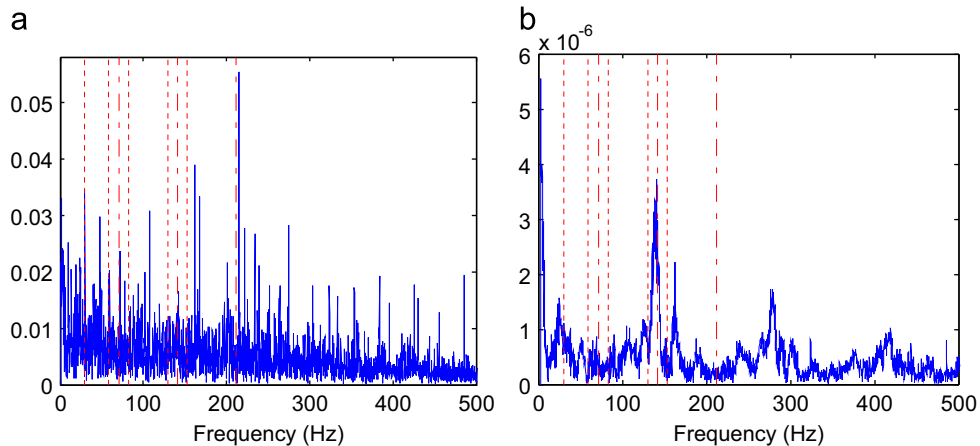


Fig. 25. Record 226DE (48k, 0.021 in. drive end ball fault, 1797 rpm). (a) Envelope spectrum from Method 1 (raw signal); N1 diagnosis. (b) Envelope spectrum from Method 2 (prewhitening); P1 diagnosis.

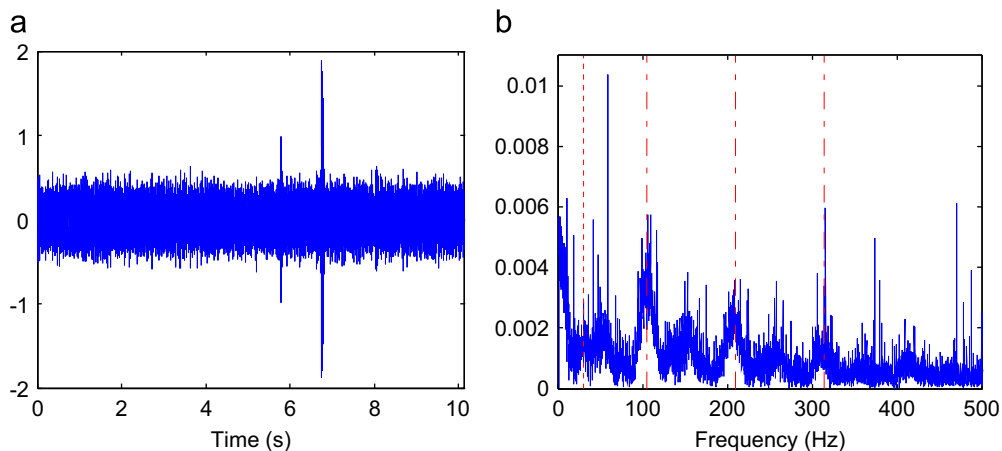


Fig. 26. Record 203DE (48k, 0.014 in. drive end outer race fault centred, 1750 rpm). (a) Raw time signal. (b) Envelope spectrum from Method 1 (raw signal); P2 diagnosis.

6.4.4. Outer race faults, fault orthogonal to load zone (3 o'clock)

As with the 12k data, the 0.007 in. faults in this category are easily diagnosable from the raw signal (all Y1 diagnoses), even though most records exhibit a mild (non-classical) modulation of the BPFO component by a combination of FTF and shaft speed. Fig. 28, from data set 148, shows these effects, and it can be seen to be very similar to the equivalent 12k record, 144, shown in Fig. 15.

The results for the 0.021 in. faults are also very similar to those of the 12k data sets, with clear diagnoses obtained directly from the raw signal despite the presence of strong shaft speed modulation of BPFO harmonics in the envelope spectrum (see Fig. 17).

6.4.5. Outer race faults, fault opposite load zone (12 o'clock)

As noted in Section 6.3.5, an outer race fault located outside the load zone should not give the usual impulse responses, but virtually all the data sets in this category (0.007 in. and 0.021 in. faults only) exhibit clear outer race fault symptoms, some even quite classical. The BPFO component is strong in all envelope spectra (all Y2 and P1 diagnoses), but the degree of modulation varies and tends to be stronger in the 0.021 in. cases. The dominant modulating frequency of the BPFO components is shaft speed, two times shaft speed or FTF. Their corresponding harmonics are also present in the envelope spectra, becoming dominant in some of the 0.021 in. cases, giving P1 rather than Y2 diagnoses. An example of this is shown in Fig. 29, which gives the envelope spectra for data sets 161 and 262, which are equivalent speed/load cases from the 0.007 in. and 0.021 in. fault sets, respectively.

6.5. Fan end bearing faults, 12 kHz data (cf. Table B4)

An interesting thing about the fan end bearings (SKF type 6203-2RS JEM deep groove) is that three of the bearing characteristic frequencies are close to integer multiples of shaft speed, with values of 4.947, 3.053 and 1.994 ($\times f_r$) for BPFI, BPFO and BSF, respectively. In some of the results, the bearing frequencies appear to lock onto these shaft harmonics, making it difficult to establish a definite diagnosis, though in others there is a small difference. Diagnostics on this sort of bearing would benefit greatly from the use of accurate harmonic cursors, which have been used here.

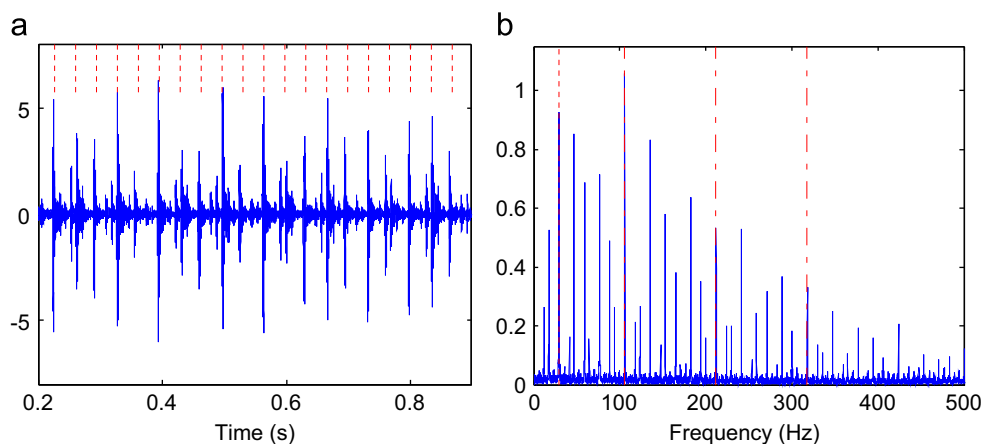


Fig. 27. Record 239DE (48k, 0.021 in. drive end outer race fault centred, 1772 rpm). (a) Raw time signal; cursors at $1/f_r$. (b) Envelope spectrum from Method 1 (raw signal); Y2 diagnosis.

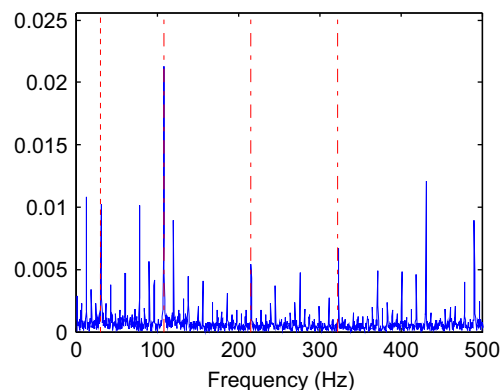


Fig. 28. Record 148FE (48k, 0.007 in. drive end outer race fault orthogonal, 1797 rpm). Envelope spectrum from Method 1 (raw signal); Y1 diagnosis.

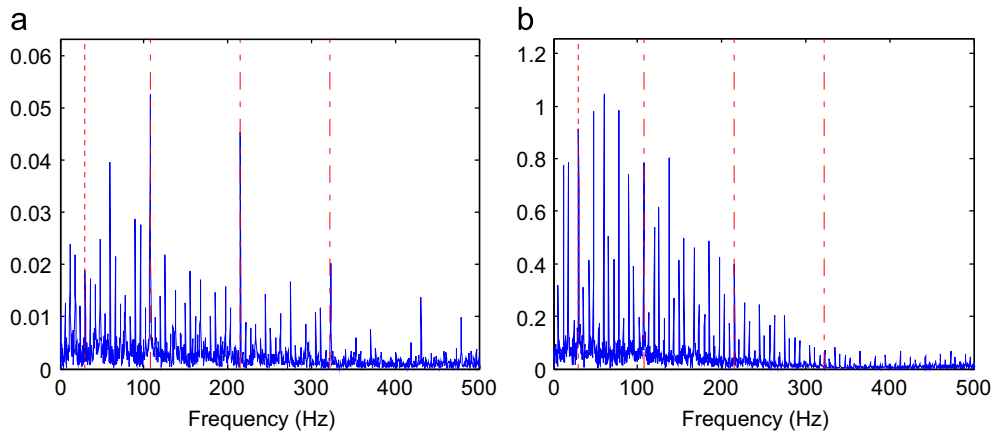


Fig. 29. Envelope spectra from Method 1 (raw signal) (48k, drive end outer race fault opposite, 1797 rpm). (a) Record 161DE (0.007 in.); Y2 diagnosis. (b) Record 262DE (0.021 in.); P1 diagnosis..

6.5.1. Inner race faults

All these faults are diagnosable with Method 1 (raw signal) applied to the fan end measurement. At other measurement points, some give a partial diagnosis by this method, and some a clear diagnosis by one of the other methods. A small number of cases (275–277, drive end measurements) are difficult to diagnose with any of the methods. It was first thought that BPFI was locking onto $5 \times f_r$ in all the records, but closer inspection with harmonic cursors revealed that the two components are indeed distinguishable.

This small difference between BPFI and $5 \times f_r$ gives rise to an interesting beat-type effect, which can be seen very clearly in Fig. 30, which is from data set 270 (for fault size 0.021 in. at the lowest load). The time record contains a series of pulses with a spacing corresponding to BPFI and subject to very impulsive modulation at shaft speed, as with many of the drive end bearing fault cases discussed previously. But the time record at first glance appears to have a series of pulses spaced at shaft speed and modulated by a mysterious low frequency (~ 1 Hz) effect. This is in fact a form of beating: at the peak of the apparent amplitude modulation function, every fifth BPFI-spaced impulse response is in phase with the peak of the shaft-speed modulation. The trough of the apparent amplitude modulation function occurs when the peak of the shaft-speed modulation falls between two BPFI-spaced pulses, and the frequency with which this cycle occurs is equal to the difference between $5 \times f_r$ and BPFI, about 0.9 Hz.

This difference can be seen clearly throughout the envelope spectrum in Fig. 30(b), where the shaft harmonics and shaft-speed sidebands from BPFI can be distinguished on close inspection. This beating effect, observed throughout the inner race fault cases, was found to be clearest on the fan end measurements and least clear on the base measurements. Although it gives an unconventional time signal, it does not impede the diagnosis based on the envelope spectrum, provided that careful use is made of harmonic cursors.

6.5.2. Ball faults

As for the drive end bearings, the ball faults are among the most difficult to diagnose, further complicated by the fact that BSF in general is indistinguishable from two times shaft speed.

Many of the cases give very different results for the three measurement points, an example of which is data set 282, for which the envelope spectra for different measurement points are compared in Fig. 31. At DE there are definite components at $2 \times$, $4 \times$ and $6 \times$ shaft speed ($1 \times$, $2 \times$, $3 \times$ BSF), with some sidebands spaced at FTF. At FE, this is not so clear, even though it is the location of the fault. At BA, the even harmonics of shaft speed, thought to be harmonics of BSF, are strong, but sidebands at FTF are very small. This pattern was found in the base measurements of a number of other data sets, and they have been categorised as Y2 diagnoses (subject to the caveat below).

While the record 282BA case (and others similar) has been classified as a successful diagnosis, there is some doubt as to the cause of the apparent BSF components. This is perhaps best explained using record 283, three envelope spectra from which are shown in Fig. 32. The envelope spectrum from the drive end measurement shows clear discrete components at $1 \times$, $2 \times$ and $3 \times$ BSF, but also less clear smeared components near $2 \times$, $4 \times$ and $6 \times$ BSF. These smeared components are quite pronounced in the envelope spectrum from the fan end, yet only discrete components are present in the envelope spectrum from the base measurements.

It was discussed in relation to the drive end bearing faults how random amplitude modulation was giving rise to smearing of the bearing fault frequencies, and inspection of the time signals shows that this is again the case here. Fig. 33 compares the time records from 283FE and 283BA, and the random amplitude modulation in the FE measurement is very clear. The large pulse just after the three second mark in fact comprises a number of impulse responses spaced at $2 \times$ BSF. By contrast, the BA record appears completely stationary. It seems quite likely, then, that the large discrete components at BSF harmonics in many of the envelope spectra from the base measurements have an alternative explanation and are not a

result of the ball fault. On consideration, however, it was decided to categorise the results *prima facie*, in which case a ball fault diagnosis would almost certainly be made.

6.5.3. Outer race faults, fault centred in load zone (6 o'clock)

Almost all of these results show some evidence of an outer race fault using Method 1 (raw signal), but often with impulsive amplitude modulation at shaft speed, most likely caused by looseness, as discussed previously for a number of

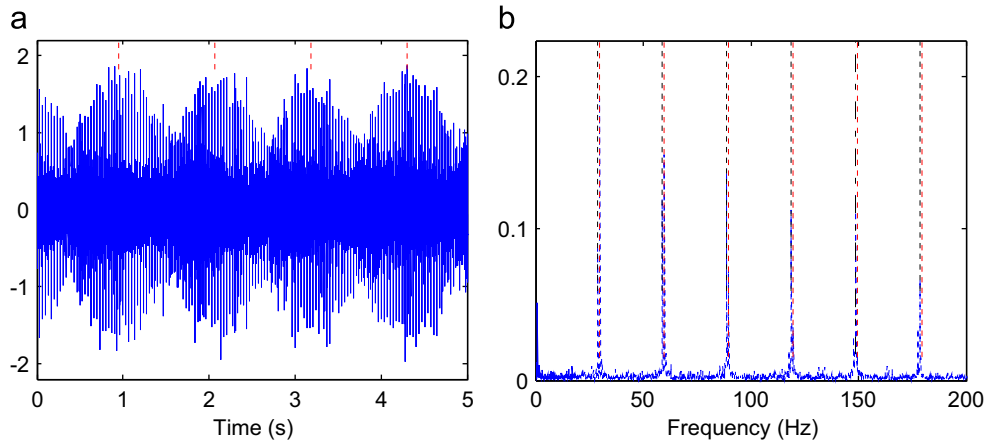


Fig. 30. Record 270FE (12k, 0.021 in. fan end inner race fault, 1797 rpm). (a) Raw time signal; cursors at 1.11 s ($= 1/[5f_r - \text{BPFI}]$). (b) Envelope spectrum from Method 1 (raw signal); finely tuned cursors at: f_r harmonics (red), BPFI (black dash-dot), f_r sidebands around BPFI (black dot); Y2 diagnosis. (For interpretation of the references to colour in this figure legend, the reader is referred to the web version of this article.)

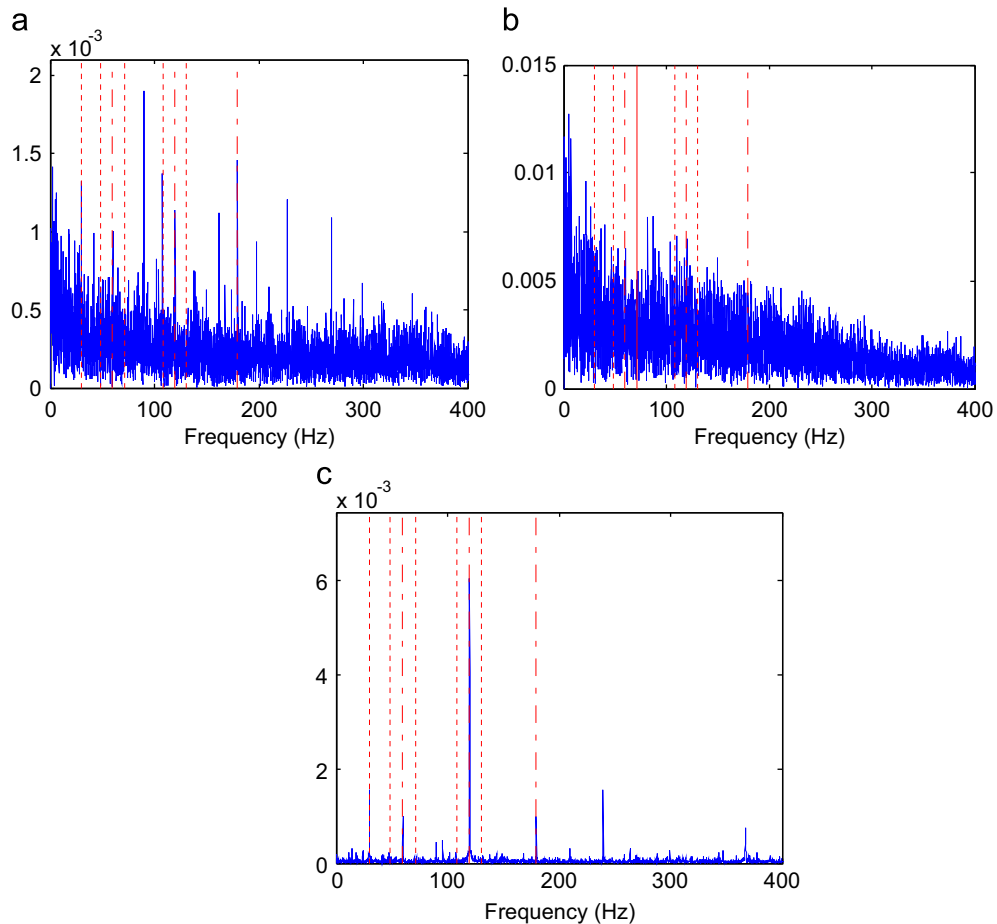


Fig. 31. Record 282 (12k, 0.007 in. fan end ball fault, 1797 rpm). Envelope spectra from Method 1 (raw signal). (a) DE; P1 diagnosis. (b) FE; N1 diagnosis. (c) BA; Y2 diagnosis.

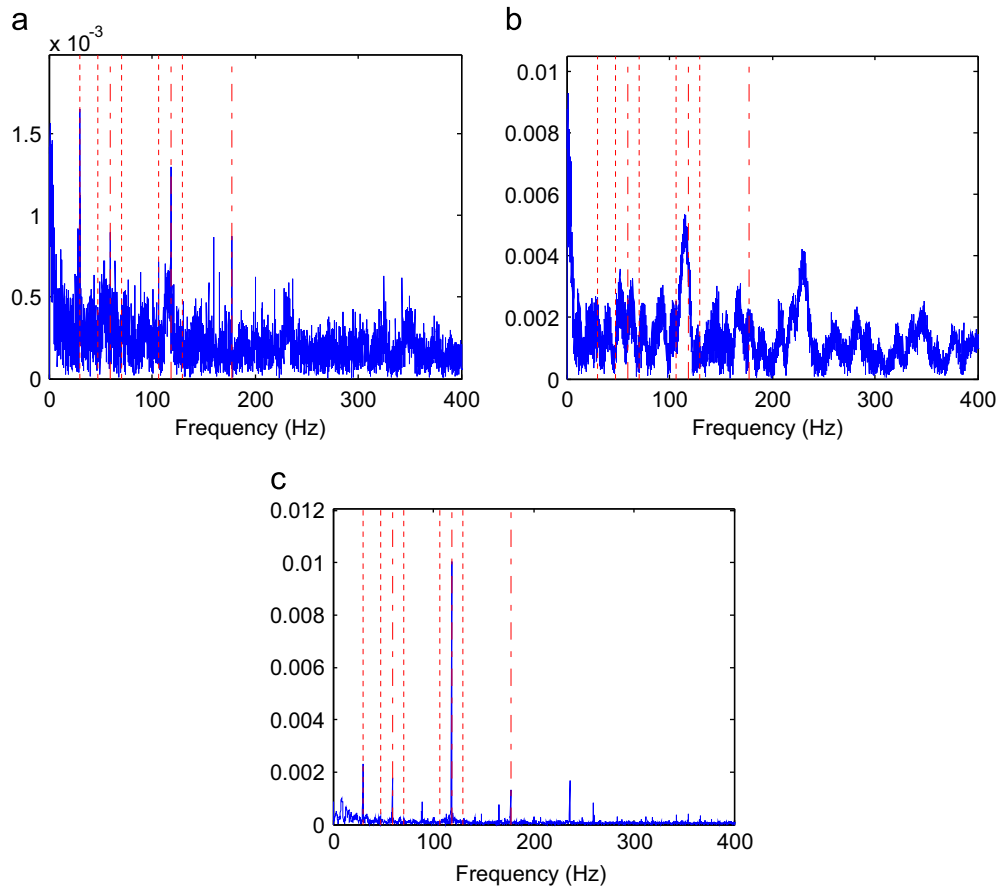


Fig. 32. Record 283 (12k, 0.007 in. fan end ball fault, 1772 rpm). Envelope spectra from Method 1 (raw signal). (a) DE; P2 diagnosis. (b) FE; P2 diagnosis. (c) BA; Y2 diagnosis.

other cases. In a manner similar to that observed with the inner race faults (Section 6.5.1), the small difference between BPFO and $3 \times$ the modulating shaft frequency gives rise to an unorthodox beating effect, a good example of which is data set 295FE, shown in Fig. 34. The time signal shows impulse responses spaced at $1/\text{BPFO}$, but very sharply modulated at shaft speed. This modulation function comes in and out of phase with every third impulse response at a rate equal to BPFO minus $3 \times f_r$, or about 2 Hz, and it is this effect that dominates the broader time record. The envelope spectrum shows a clear pattern of harmonics of BPFO surrounded by sidebands spaced at shaft speed, as well as low harmonics of shaft speed.

A few base measurement cases in this category were not diagnosable with Method 1 (raw signal), but were successfully diagnosed with Methods 2 or 3 (prewhitening or benchmark), meaning that a Y2 diagnosis was ultimately achieved for all measurement records.

6.5.4. Outer race faults, fault orthogonal to load zone (3 o'clock)

Many of these signals are not diagnosable from the raw signal, specifically with the 0.007 in. fault size. Most of the others have harmonics and sidebands associated with looseness, even if BPFO is present.

Fig. 35, from data set 311 (0.014 in. fault size), shows typical results for Method 1 (raw signal), where evidence of looseness is present in both time signal and envelope spectrum (Fig. 35(a and b)). This is one of the cases where the signal processed by Method 2 (cepstrum prewhitening) reduces the effects of looseness, and gives a definite diagnosis of outer race fault (Y1 diagnosis), as shown in Fig. 35(c and d). Many other results are similar, especially for the 0.014 in. and 0.021 in. fault sizes.

Also of note is that clear evidence of both outer and inner race faults in the drive end bearing was observed in some of the drive end measurements from the 0.007 in. (fan end) fault. An example is given in Fig. 36, from data set 298, where the fan end fault is not detectable but there are very clear harmonics of BPFO and BPFI from the drive end bearing (approximately 107.7 and 161.8 Hz, respectively).

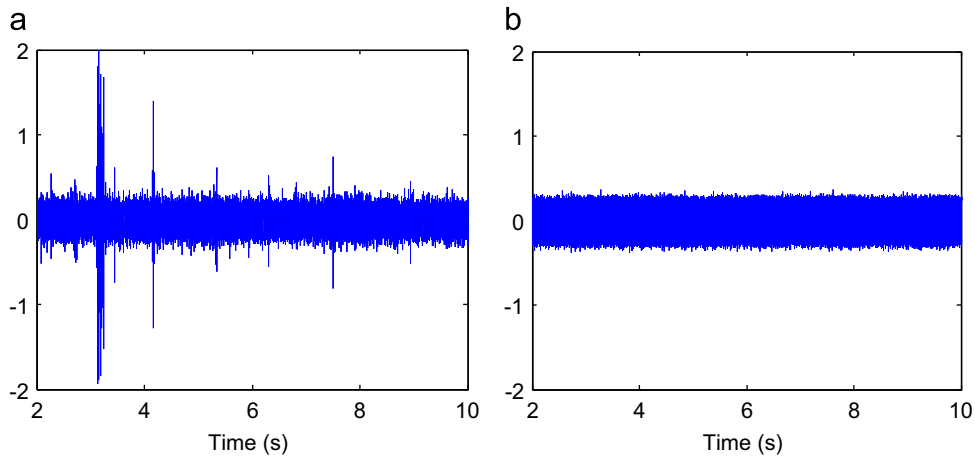


Fig. 33. Record 283 (12k, 0.007 in. fan end ball fault, 1772 rpm). Raw time signals (a) FE and (b) BA.

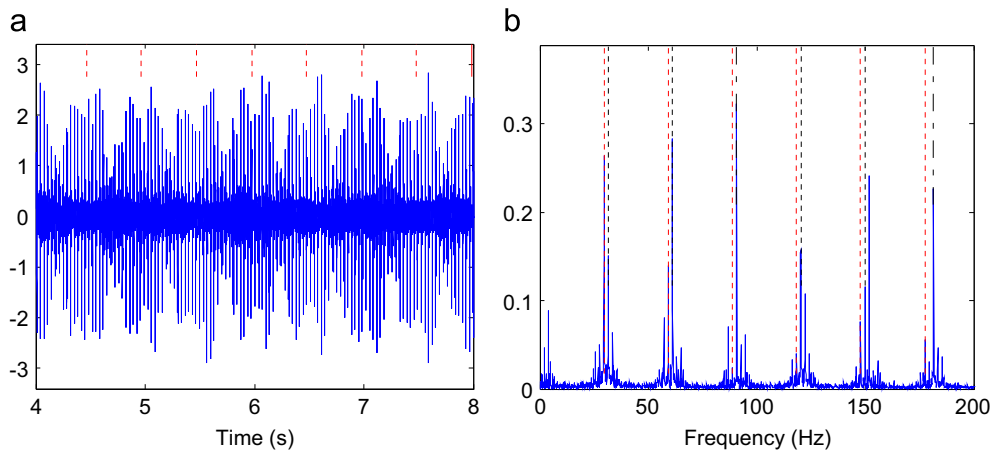


Fig. 34. Record 295FE (12k, 0.007 in. fan end outer race fault centred, 1772 rpm). Raw time signal; cursors at $0.50\text{ s} (= 1/(BPFO - 3f_r))$. (b) Envelope spectrum from Method 1 (raw signal); finely tuned cursors at: f_r harmonics (red), BPFO harmonics (black dash-dot), f_r sidebands around BPFO (black dot); Y2 diagnosis. (For interpretation of the references to colour in this figure legend, the reader is referred to the web version of this article.)

6.5.5. Outer race faults, fault opposite load zone (12 o'clock)

None of these signals are clearly diagnosable with any of the techniques applied, though two partial diagnoses were given. Extreme nonstationarity – likely from looseness – is again a feature of some of the records. Fig. 37, from data set 305DE, shows a P2 diagnosis given using Method 1 (raw signal). The envelope spectrum contains a discrete component at BPFO, but it is not a very convincing diagnosis. The corresponding time record shows one particularly large pulse, which is in fact two separate pulses spaced at about 0.015 s, or 67 Hz, which is likely the cause of the broadened humps at harmonics of this frequency in the envelope spectrum. This does not seem to be related to any bearing faults, however. As with record 298 (Fig. 36), outer and inner race faults in the drive end bearing are again apparent here (at 106.4 and 159.8 Hz).

6.6. Further discussion

It was suggested in Section 6.1.1 that due to the presence of discrete components at high frequencies, the 12k data sets may be easier to diagnose, but in fact the overall diagnostic outcomes for the 12k and 48k data sets were found to be very similar.

As for the applied methods, Method 2 (cepstrum prewhitening) was actually found to perform the best overall, followed closely by Method 3 (benchmark). Fig. 38 shows a summary of the diagnosis outcomes for the more challenging data sets, for which Method 1 (raw signal) was unsuccessful for at least one measurement point. In the figure, the N1 and N2 diagnoses have been combined under the category 'N'. It can be seen that Methods 2 and 3 give a similar number of partial diagnoses (P1 and P2), but that Method 2 gives a greater number of successful results (Y1 and Y2). One reason the

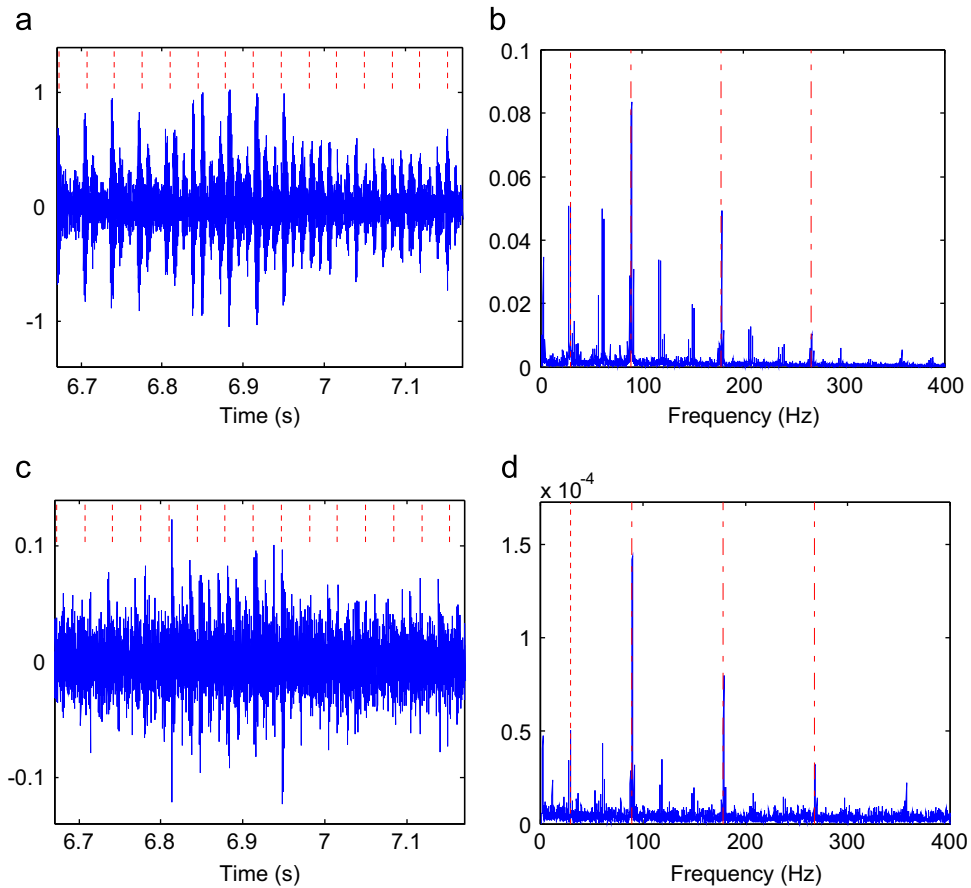


Fig. 35. Record 311 (12k, 0.014 in. fan end outer race fault orthogonal, 1750 rpm). (a) Raw time signal; cursors at $1/f_r$, (b) Envelope spectrum from Method 1 (raw signal); Y2 diagnosis, (c) Time signal from Method 2 (prewhitening); cursors at $1/f_r$, and (d) Corresponding envelope spectrum; Y1 diagnosis.

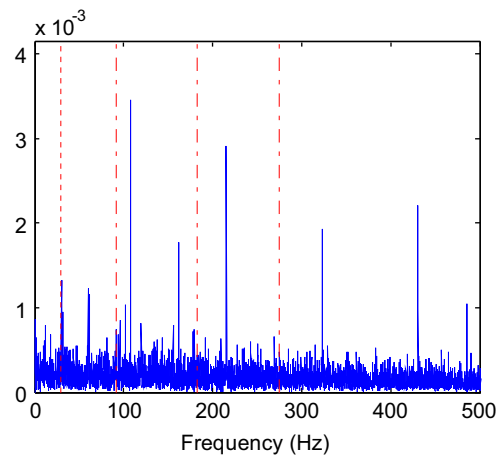


Fig. 36. Record 298DE (12k, 0.007 in. fan end outer race fault orthogonal, 1797 rpm). Envelope spectrum from Method 1 (raw signal); N1 diagnosis.

benchmark method may not have performed quite so well overall is due to the presence in many of the data sets of ‘impulsive noise’, i.e. impulsive content unrelated to the specified bearing fault. Spectral kurtosis (applied only in Method 3) is vulnerable to impulsive noise, tending to enhance individual impulses over series of transients (as would occur with a bearing fault). A new method recently proposed by Antoni may be capable of dealing with such challenges [14].

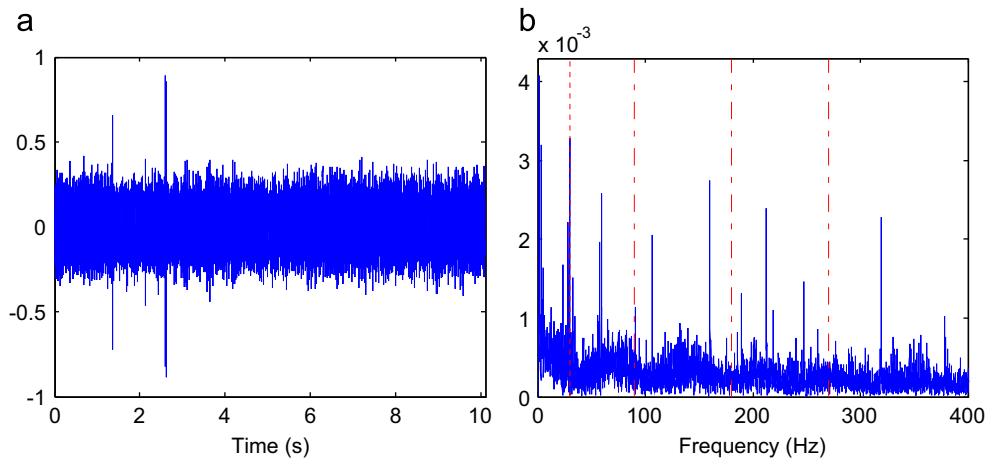


Fig. 37. Record 305DE (12k, 0.007 in. fan end outer race fault opposite, 1772 rpm). (a) Raw time signal. (b) Envelope spectrum from Method 1 (raw signal); P2 diagnosis.

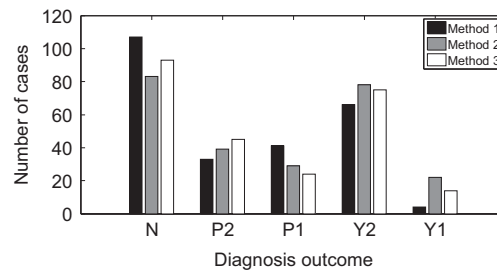


Fig. 38. Method comparison: diagnosis outcomes for the more difficult data sets.

6.7. Summary of results

The complete results set in Appendix B shows a range of diagnosis outcomes, ranging from faults exhibiting classical symptoms (Y1 diagnosis) to those found to be undiagnosable with the applied methods (N1 or N2 diagnosis). To summarise the results, the data sets in these extreme categories are listed in Tables 5 and 6, respectively.

Data sets in Table 5, giving classical symptoms, might be of use for research into areas such as spall size determination, or they could be considered valid training sets for machine learning algorithms. On the other hand, the undiagnosable records listed in Table 6 might provide a robust test for any newly proposed diagnostic algorithms.

7. Conclusions and recommendations

This study used three established bearing diagnostic techniques to provide a benchmark analysis of the widely used data set from the Case Western Reserve University (CWRU) Bearing Data Center. It was found that the data records ranged from very easily diagnosable – using simple envelope analysis of the raw signal – to not diagnosable with any of the applied methods. It was also found that relatively few of the records gave classical characteristics for the specified bearing fault type. A central finding of the analysis was that in many cases the test rig assembly seemed to affect the diagnosis results more than the fault itself, with evidence of mechanical looseness observed in many of the data sets. A number of data sets also exhibited very non-stationary characteristics, with the given bearing faults manifesting themselves in only small patches of the signal; this is perhaps an area that could be addressed in future algorithm development.

With respect to testing new diagnostic algorithms, it is recommended that researchers demonstrate the relative advantages of their proposed method against the benchmark results in this study. This could include obtaining a more comprehensive diagnosis for data sets that were only partially or unsuccessfully diagnosed here, or by achieving similar results using methods with other comparative advantages, e.g. computational efficiency. For a proper assessment of any new algorithms, it is also recommended that researchers specify the record number and measurement point for the data set(s) on which their results are based.

For researchers considering generating new benchmark data for bearing diagnostics, it is recommended that they follow a systematic and comprehensive approach to documentation, as provided by the CWRU Bearing Data Center. Yet much of the CWRU data was found here to be atypical, and any future attempt to generate data should consider the specific problems outlined in this paper. Before dissemination, the data should be thoroughly examined using established bearing diagnostic

Table 5

Data sets giving classical fault symptoms with at least one method (Y1 diagnosis).

Fault type					
	IR	Ball	OR centred	OR orthogonal	OR opposite
Drive end bearing faults 12 kHz data	209DE, 209FE ^a , 210DE, 211DE, 212DE	–	130, 131, 132, 133	144DE ^a , 144BA, 145DE ^a , 145FE, 145BA, 146DE ^a , 146FE ^b , 146BA ^b , 147DE ^a , 147FE, 147BA	156DE ^a , 156FE ^a , 159DE ^a , 160DE ^a
Drive end bearing faults 48 kHz data	213, 215FE ^a	–	135, 136, 137, 138	148, 149, 150, 151	161DE ^a , 162 ^a , 163DE ^{ab} , 164 ^{ab}
Fan end bearing faults 12 kHz data	278DE, 278FE ^b , 279DE ^b , 280DE ^b , 280BA ^b , 281DE ^b , 274FE, 275FE ^a , 276FE ^a , 276BA ^a , 277FE ^{a,b} , 277BA ^a , 271DE ^a , 271FE ^{ab} , 271BA ^a , 272DE ^{a,b} , 272FE ^a , 272BA ^a , 273DE ^{a,b} , 273FE, 273BA ^a	–	313DE ^a , 313FE ^a , 315DE ^a	310DE ^a , 310FE ^a , 309DE ^b , 311DE ^a , 311FE ^a , 312DE ^a , 312FE ^a , 317DE, 317FE, 317BA ^b	–

Unmarked cases achieved Y1 diagnosis with Method 1 (raw signal).

^a Y1 diagnosis achieved with Method 2 (cepstrum prewhitening) but not with Method 1.^b Y1 diagnosis achieved with Method 3 (benchmark) but not with Method 1.**Table 6**

Data sets not diagnosable with any of the applied methods (only N1 or N2 diagnoses).

Fault type					
	IR	Ball	OR centred	OR ortho- nal	OR opposite
Drive end bearing faults 12 kHz data	3001, 3002, 3003, 3004	118, 119, 120DE, 120BA, 121BA, 187FE, 224DE, 224BA, 225DE, 225FE	197FE, 197BA, 198FE, 198BA, 199FE, 200	–	–
Drive end bearing faults 48 kHz data	174	122, 123, 124, 125, 192, 228DE, 229DE	202FE, 204FE	–	–
Fan end bearing faults 12 kHz data	–	282FE, 285FE, 290DE, 290FE, 292FE, 293DE	–	298BA	302, 305FE, 306, 307

techniques. Faults in bearings often manifest themselves at high frequencies, so the use of a high sampling rate – perhaps greater than 40 kHz – is recommended. One area of particular interest at present is diagnostics under variable speed conditions, and for such cases an angular reference signal, for example from a tachometer or shaft encoder, would be essential.

Acknowledgements

This research was supported by the Australian Research Council and SpectraQuest, through Linkage Project [LP110200738]. The authors would like to thank the Case Western Reserve University Bearing Data Center for providing the data for this study.

Appendix A. Data set reference tables

Tables A1–A4.

Table A148 k normal baseline data; $f_s=48$ kHz; variables recorded: DE and FE.

Motor load hp	Shaft speed rpm	Data set number
0	1797	97
1	1772	98
2	1750	99
3	1730	100

DE=drive end acceleration; FE=fan end acceleration.

Table A212 k drive end bearing fault data; $f_s=12$ kHz; variables recorded: DE, FE and BA (0.007 in.–0.021 in. faults); DE (0.028 in. fault).

Fault width in. (mm)	Motor load hp	Shaft speed rpm	Data set number for each fault type				
			IR	Ball	OR centred	OR orthogonal	OR opposite
0.007(0.18)	0	1797	105	118	130	144	156
	1	1772	106	119	131	145	158
	2	1750	107	120	132	146	159
	3	1730	108	121	133	147	160
0.014(0.36)	0	1797	169	185	197	—	—
	1	1772	170	186	198	—	—
	2	1750	171	187	199	—	—
	3	1730	172	188	200	—	—
0.021 (0.53)	0	1797	209	222	234	246	258
	1	1772	210	223	235	247	259
	2	1750	211	224	236	248	260
	3	1730	212	225	237	249	261
0.028 (0.71)	0	1797	3001	3005	—	—	—
	1	1772	3002	3006	—	—	—
	2	1750	3003	3007	—	—	—
	3	1730	3004	3008	—	—	—

DE=drive end acceleration; FE=fan end acceleration; BA=base plate acceleration.

Table A348 k drive end bearing fault data; $f_s=48$ kHz; variables recorded: DE and FE.

Fault width in (mm)	Motor load hp	Shaft speed rpm	Data set number for each fault type				
			IR	Ball	OR centred	OR orthogonal	OR opposite
0.007 (0.18)	0	1797	109	122	135	148	161
	1	1772	110	123	136	149	162
	2	1750	111	124	137	150	163
	3	1730	112	125	138	151	164
0.014 (0.36)	0	1797	174	189	201	—	—
	1	1772	175	190	202	—	—
	2	1750	176	191	203	—	—
	3	1730	177	192	204	—	—
0.021 (0.53)	0	1797	213	226	238	250	262
	1	1772	214	227	239	251	263
	2	1750	215	228	240	252	264
	3	1730	217	229	241	253	265

DE=drive end acceleration; FE=fan end acceleration.

Table A412 k fan end bearing fault data; $f_s=12$ kHz; variables recorded: DE, FE and BA.

Fault width in (mm)	Motor load hp	Shaft speed rpm	Data set number for each fault type				
			IR	Ball	OR centred	OR orthogonal	OR opposite
0.007 (0.18)	0	1797	278	282	294	298	302
	1	1772	279	283	295	299	305
	2	1750	280	284	296	300	306
	3	1730	281	285	297	301	307
0.014 (0.36)	0	1797	274	286	313	310	—
	1	1772	275	287	—	309	—
	2	1750	276	288	—	311	—
	3	1730	277	289	—	312	—
0.021 (0.53)	0	1797	270	290	315	—	—
	1	1772	271	291	—	316	—
	2	1750	272	292	—	317	—
	3	1730	273	293	—	318	—

DE=drive end acceleration; FE=fan end acceleration; BA=base plate acceleration.

Appendix B. Results tables

Tables B1–B4.

Table B1

48 k normal baseline data analysis results; kurtosis: DE only.

Data set	Kurtosis
97	2.76
98	2.93
99	2.93
100	2.96

DE=drive end acceleration.

Table B2

12 k drive end bearing fault analysis results; kurtosis: DE only; diagnosis: DE/FE/BA (0.007 in. –0.021 in. faults), DE (0.028 in. fault).

Inner race faults					Ball faults				
Data set	Kurtosis	Diagnosis category			Data set	Kurtosis	Diagnosis category		
		M1	M2	M3			M1	M2	M3
105	5.40	Y2/Y2/Y2			118	2.98	N1/N2/N2	N1/N2/N2	N1/N2/N2
106	5.54	Y2/Y2/Y2			119	2.96	N1/N1/N1	N2/N2/N2	N1/N1/N2
107	5.56	Y2/Y2/Y2			120	2.83	N1/N2/N2	N2/N2/N2	N1/P2/N2
108	5.29	Y2/Y2/Y2			121	2.89	N1/N1/N1	N1/P2/N1	Y2/P2/N1
169	22.0	Y2/Y2/N2	Y2/Y2/P1	Y2/Y2/P1	185	17.8	P2/N1/N1	P2/P2/P2	N1/P2/P2
170	22.1	Y2/Y2/P1	Y2/Y2/P1	Y2/P1/P1	186	8.84	P2/N1/N1	P2/P2/P2	P2/N1/P2
171	21.7	P1/P1/N2	Y2/P1/P1	Y2/P1/P1	187	9.75	N1/N1/N1	P2/N1/N1	N1/N1/P2
172	18.2	Y2/P1/N2	Y2/P1/P1	Y2/P1/P1	188	14.9	P2/N1/N1	P2/P2/P2	P2/P2/P2
209	7.45	Y1/Y2/Y2			222	8.55	P1/P2/N1	Y2/Y2/Y2	Y2/P2/Y2
210	7.67	Y1/Y2/Y2			223	9.41	Y2/Y2/P2	Y2/Y2/Y2	P2/Y2/Y2
211	8.06	Y1/Y2/Y2			224	3.30	N1/N1/N1	N1/N1/N1	N1/P2/N1
212	8.35	Y1/Y2/Y2			225	3.11	N1/N1/N1	N1/N1/N1	N1/N1/P2
3001	3.40	N1/–/–	N1/–/–	N1/–/–	3005	3.87	Y2/–/–		
3002	3.20	N1/–/–	N1/–/–	N1/–/–	3006	3.91	Y2/–/–		
3003	3.29	N1/–/–	N1/–/–	N1/–/–	3007	3.77	Y2/–/–		
3004	3.32	N1/–/–	N1/–/–	N1/–/–	3008	3.90	Y2/–/–		
Outer race faults (centred)					Outer race faults (orthogonal)				
Data set	Kurtosis	Diagnosis category			Data set	Kurtosis	Diagnosis category		
		M1	M2	M3			M1	M2	M3
130	7.65	Y1/Y1/Y1			144	4.24	Y2/Y2/Y1		
131	7.60	Y1/Y1/Y1			145	4.05	Y2/Y1/Y1		
132	7.85	Y1/Y1/Y1			146	3.94	Y2/Y2/Y2		
133	7.96	Y1/Y1/Y1			147	4.09	Y2/Y1/Y1		
197	3.06	N1/N1/N1	N1/N2/N2	Y2/N1/N1	–	–	–	–	–
198	2.94	P2/N2/N1	N2/N2/N2	N2/N2/N2	–	–	–	–	–
199	3.02	P1/N2/N1	N2/N2/N2	N2/N1/P2	–	–	–	–	–
200	3.80	N1/N1/N1	N1/N1/N1	N1/N1/N1	–	–	–	–	–
234	21.0	Y2/Y2/Y2			246	6.95	Y2/Y2/P1	Y2/Y2/Y2	Y2/Y2/Y2
235	22.0	Y2/Y2/Y2			247	7.10	Y2/Y2/P1	Y2/Y2/Y2	Y2/Y2/Y2
236	23.2	Y2/Y2/Y2			248	6.86	Y2/Y2/Y2		
237	23.5	Y2/Y2/Y2			249	6.38	Y2/Y2/Y2		
					Outer race faults (opposite)				
Data set	Kurtosis	Diagnosis category			Data set	Kurtosis	Diagnosis category		
		M1	M2	M3			M1	M2	M3
156	8.05	Y2/Y2/P1	Y1/Y1/Y2	Y2/Y2/Y2	158	8.02	Y2/Y2/P1	Y2/Y2/Y2	Y2/Y2/N2
159	8.66	Y2/Y2/Y2			160	8.29	Y2/Y2/Y2		
–	–	–	–	–	–	–	–	–	–
–	–	–	–	–	–	–	–	–	–
–	–	–	–	–	–	–	–	–	–
–	–	–	–	–	–	–	–	–	–
258	35.0	Y2/P1/Y2	Y2/P1/P1	Y2/Y2/Y2	259	33.7	Y2/P1/Y2	Y2/P1/Y2	Y2/P1/Y2
260	33.8	Y2/P1/Y2	Y2/P1/Y2	Y2/Y2/Y2	261	33.1	Y2/Y2/Y2		

DE=drive end acceleration; FE=fan end acceleration; BA=base plate acceleration; M1–3=Method 1–3; diagnosis categories described in Section 6.2.

Table B3

48 k drive end bearing fault analysis results; kurtosis: DE only; diagnosis: DE/FE.

Inner race faults					Ball faults				
Data set	Kurtosis	Diagnosis category			Data set	Kurtosis	Diagnosis category		
		M1	M2	M3			M1	M2	M3
109	6.03	Y2/Y2	—	—	122	3.15	N1/N2	N2/N2	N1/N2
110	7.37	Y2/Y2	—	—	123	3.07	N1/N1	N2/N2	N1/N1
111	7.51	Y2/Y2	—	—	124	3.09	N1/N1	N2/N1	N1/N2
112	6.83	Y2/Y2	—	—	125	3.04	N1/N1	N2/N1	N1/N2
174	11.7	N1/N1	N1/N1	N1/N1	189	10.2	N1/N1	P2/P2	P2/P2
175	19.3	P1/Y2	Y2/Y2	Y2/P1	190	18.1	N1/N1	P2/P2	N1/P2
176	20.2	P1/P1	Y2/Y2	P1/P2	191	37.7	N1/N1	P2/P2	N1/P2
177	14.9	P1/P1	Y2/Y2	N1/N1	192	17.1	N1/N1	N1/N1	N1/N1
213	4.17	Y1/Y1	—	—	226	3.22	N1/N1	P1/P1	N1/N1
214	3.94	Y2/Y2	—	—	227	9.94	P2/P2	P1/P1	P2/P2
215	3.65	Y2/Y2	—	—	228	16.8	N1/N1	N1/P1	N1/N1
217	3.65	Y2/Y2	—	—	229	18.6	N1/N1	N1/P1	N1/P2
Outer race faults (centred)					Outer race faults (orthogonal)				
Data set	Kurtosis	Diagnosis category			Data set	Kurtosis	Diagnosis category		
		M1	M2	M3			M1	M2	M3
135	6.74	Y1/Y1	—	—	148	4.16	Y1/Y1	—	—
136	6.86	Y1/Y1	—	—	149	4.11	Y1/Y1	—	—
137	6.94	Y1/Y1	—	—	150	4.38	Y1/Y1	—	—
138	7.39	Y1/Y1	—	—	151	4.10	Y1/Y1	—	—
201	3.77	Y2/Y2	—	—	—	—	—	—	—
202	3.68	P1/N2	N1/N1	P1/N1	—	—	—	—	—
203	6.02	P2/N1	P2/P2	P2/N1	—	—	—	—	—
204	3.00	Y2/N2	N2/N1	Y2/N1	—	—	—	—	—
238	20.8	Y2/Y2	—	—	250	8.36	Y2/Y2	—	—
239	20.5	Y2/Y2	—	—	251	7.31	Y2/Y2	—	—
240	21.0	Y2/Y2	—	—	252	7.20	Y2/Y2	—	—
241	19.8	Y2/Y2	—	—	253	7.54	Y2/Y2	—	—
					Outer race faults (opposite)				
Data set	Kurtosis	Diagnosis category			Data set	Kurtosis	Diagnosis category		
		M1	M2	M3			M1	M2	M3
161	5.49	Y2/Y2	—	—	161	5.49	Y2/Y2	—	—
162	12.4	Y2/Y2	—	—	162	12.4	Y2/Y2	—	—
163	11.6	Y2/Y2	—	—	163	11.6	Y2/Y2	—	—
164	10.1	Y2/Y2	—	—	164	10.1	Y2/Y2	—	—
—	—	—	—	—	—	—	—	—	—
—	—	—	—	—	—	—	—	—	—
—	—	—	—	—	—	—	—	—	—
—	—	—	—	—	—	—	—	—	—
262	25.6	P1/P1	Y2/P1	Y2/P1	262	25.6	P1/P1	Y2/P1	Y2/P1
263	22.9	Y2/P1	Y2/Y2	Y2/Y2	263	22.9	Y2/P1	Y2/Y2	Y2/Y2
264	22.6	P1/P1	Y2/P1	P1/P1	264	22.6	P1/P1	Y2/P1	P1/P1
265	21.1	Y2/P1	Y2/P1	Y2/P1	265	21.1	Y2/P1	Y2/P1	Y2/P1

DE=drive end acceleration; FE=fan end acceleration; M1–3=Method 1–3; diagnosis categories described in Section 6.2

Table B4

12 k fan end bearing fault analysis results; kurtosis: DE only; diagnosis: DE/FE/BA.

Inner race faults					Ball faults				
Data set	Kurtosis	Diagnosis category			Data set	Kurtosis	Diagnosis category		
		M1	M2	M3			M1	M2	M3
278	4.01	Y1/Y2/P1	Y2/Y2/Y2	Y1/Y1/N2	282	3.87	P1/N1/Y2	P2/N1/N1	N1/N1/P1
279	3.91	Y2/Y2/N1	Y2/Y2/Y2	Y1/Y2/Y2	283	3.98	P2/P2/Y2	P2/P2/N1	N1/P2/N1
280	3.87	Y2/Y2/N1	Y2/Y2/Y2	Y1/Y2/Y1	284	3.59	N1/P2/Y2	Y2/Y2/Y2	P2/P2/N1
281	3.70	Y2/Y2/N1	Y2/Y2/Y2	Y1/P1/Y2	285	5.90	P1/N1/Y2	N1/N1/N1	P1/N1/Y2
274	3.71	Y2/Y1/Y2	—	—	286	11.4	P2/P2/P1	P2/P2/P2	P2/P2/N1
275	4.26	P1/Y2/P2	P1/Y1/Y2	N1/Y2/N1	287	12.9	P2/P2/Y2	P2/P2/P2	P2/P2/N1
276	4.44	P1/Y2/P2	P1/Y1/Y1	N1/Y2/Y2	288	8.11	P2/P2/Y2	P1/P2/P2	P2/P2/P2
277	4.76	P1/Y2/N1	P1/Y1/Y1	P1/Y1/Y2	289	9.14	P2/P2/Y2	P2/P2/P2	P2/P2/N1
270	4.65	P1/Y2/P2	Y2/Y2/Y2	Y2/Y2/P2	290	3.47	N1/N1/Y2	N1/N1/N1	N1/N1/N1
271	3.96	P1/Y2/P1	Y1/Y1/Y1	Y2/Y1/Y2	291	3.93	P2/P2/Y2	N1/N1/N1	P2/P2/N1
272	3.74	Y2/Y2/P1	Y1/Y1/Y1	Y1/Y2/Y2	292	3.44	N1/N1/Y2	P2/N1/N1	N1/N1/P2
273	3.64	P1/Y1/P2	Y1/Y1/Y1	Y1/Y1/Y2	293	3.25	N1/N1/Y2	N1/P2/P2	N1/P2/N1
Outer race faults (centred)					Outer race faults (orthogonal)				
Data set	Kurtosis	Diagnosis category			Data set	Kurtosis	Diagnosis category		
		M1	M2	M3			M1	M2	M3
294	6.47	Y2/Y2/P1	Y2/Y2/Y2	Y2/Y2/P1	298	3.24	N1/P2/N1	N2/P1/N1	P2/P1/N1
295	7.67	Y2/Y2/P2	Y2/Y2/Y2	Y2/Y2/P2	299	3.17	P2/P1/N1	P1/P1/P1	N1/P1/Y2
296	7.81	Y2/Y2/P2	Y2/Y2/Y2	Y2/Y2/Y2	300	3.13	P2/N1/N1	P2/P1/N1	N2/P1/P2
297	7.97	Y2/Y2/N1	Y2/Y2/Y2	Y2/Y2/Y2	301	3.07	N1/N2/N1	P2/P2/P1	N1/P2/Y2
313	5.49	Y2/Y2/Y2	—	—	310	6.29	Y2/Y2/Y2	—	—
—	—	—	—	—	309	3.80	Y2/Y2/Y2	—	—
—	—	—	—	—	311	4.90	Y2/Y2/P1	Y1/Y1/Y2	Y2/Y2/Y2
—	—	—	—	—	312	4.75	Y2/Y2/P1	Y1/Y1/Y2	Y2/Y2/Y2
315	5.87	Y2/Y2/Y2	—	—	—	—	—	—	—
—	—	—	—	—	316	3.42	Y2/Y2/P2	Y2/Y2/Y2	Y2/Y2/Y2
—	—	—	—	—	317	3.33	Y1/Y1/N1	Y1/Y1/Y2	Y1/Y1/Y1
—	—	—	—	—	318	3.79	Y2/Y2/N1	Y2/Y2/Y2	Y2/Y2/N1

DE=drive end acceleration; FE=fan end acceleration; BA=base plate acceleration; M1–3=Method 1–3; diagnosis categories described in Section 6.2

References

- [1] R.B. Randall, J. Antoni, Rolling element bearing diagnostics – a tutorial, *Mech. Syst. Signal Process.* 25 (2011) 485–520.
- [2] Case Western Reserve University Bearing Data Center Website (<http://csegroups.case.edu/bearingdatacenter/home>).
- [3] P.D. McFadden, J.D. Smith, Model for the Vibration Produced by a Single Point Defect in a Rolling Element Bearing, *J. Sound Vib.* 96 (1984) 69–82.
- [4] W. Du, J. Tao, Y. Li, C. Liu, Wavelet leaders multifractal features based fault diagnosis of rotating mechanism, *Mech. Syst. Signal Process.* 43 (2014) 57–75.
- [5] L. Jiang, J. Xuan, T. Shi, Feature extraction based on semi-supervised kernel Marginal Fisher analysis and its application in bearing fault diagnosis, *Mech. Syst. Signal Process.* 41 (2013) 113–126.
- [6] N. Sawalhi, R.B. Randall, Signal Prewhitening using Cepstrum Editing (Liftering) to Enhance Fault Detection in Rolling Element Bearings, COMADEM, Stavanger, Norway, 2011.
- [7] P. Borghesani, P. Pennacchi, R.B. Randall, N. Sawalhi, R. Ricci, Application of cepstrum pre-whitening for the diagnosis of bearing faults under variable speed conditions, *Mech. Syst. Signal Process.* 36 (2013) 370–384.
- [8] N. Sawalhi, Diagnostics, Prognostics and Fault Simulation For Rolling Element Bearings, The University of New South Wales, 2007 Ph.D. thesis.
- [9] J. Antoni, R.B. Randall, Unsupervised noise cancellation for vibration signals: part II—a novel frequency-domain algorithm, *Mech. Syst. Signal Process.* 18 (2004) 103–117.
- [10] J. Antoni, Fast computation of the kurtogram for the detection of transient faults, *Mech. Syst. Signal Process.* 21 (2007) 108–124.
- [11] W. Smith, L. Deshpande, R. Randall, H. Li, Bearing diagnostics in a planetary gearbox: a study using internal and external vibration signals, COMADEM, Helsinki, Finland, 2013.
- [12] K. Detrich, N. Sawalhi, S. Ganeriwala, The Interference of Variable Frequency Drives (VFDs) on the Vibration Signature Analysis of Machine Defects, CM & MFPT, Kraków, Poland, 2013 (also available as a SpectraQuest Technote at http://spectraquest.com/technote_display/?technote_id=37).
- [13] T.A. Harris, M.N. Kotzalas, *Advanced Concepts of Bearing Technology* (in Rolling Bearing Analysis, Fifth Edition), CRC Press, Boca Raton, 2006.
- [14] J. Antoni, Optimization of the envelope spectrum with the entropic uncertainty principle, ISMA2014, Leuven, Belgium, 2014, 379–391.